Research Paper

THEMED ISSUE: Tectonic, Sedimentary, Volcanic, and Fluid Flow Processes along the Queen Charlotte–Fairweather Fault System and Surrounding Continental Margin

GEOSPHERE

GEOSPHERE, v. 16, no. 6

https://doi.org/10.1130/GES02269.1

11 figures; 3 tables; 1 set of supplemental files

CORRESPONDENCE: nprouty@usgs.gov

CITATION: Prouty, N.G., Brothers, D.S., Kluesner, J.W., Barrie, J.V., Andrews, B.D., Lauer, R.M,, Greene, H.G., Conrad, J.E., Lorenson, T.D., Law, M.D., Sahy, D., Conway, K., McGann, M.L., and Dartnell, P., 2020, Focused fluid flow and methane venting along the Queen Charlotte fault, offshore Alaska (USA) and British Columbia (Canada): Geosphere, v. 16, no. 6, p. 1336–1357, https://doi.org/10.1130/GES02269.1.

Science Editor: Shanaka de Silva

Received 8 April 2020
Revision received 15 July 2020
Accepted 21 September 2020

Published online 2 November 2020

GOLD OPEN ACCESS

THE GEOLOGICAL SOCIETY OF AMERICA®

This paper is published under the terms of the CC-BY-NC license.

© 2020 The Authors

# Focused fluid flow and methane venting along the Queen Charlotte fault, offshore Alaska (USA) and British Columbia (Canada)

**Nancy G. Prouty[1], Daniel S. Brothers[1], Jared W. Kluesner[1], J. Vaughn Barrie[2], Brian D. Andrews[3], Rachel M. Lauer[4], H. Gary Greene[5], James E. Conrad[1], Thomas D. Lorenson[1], Michael D. Law[4], Diana Sahy[6], Kim Conway[2], Mary L. McGann[1], and Peter Dartnell[1]**

[1]Pacific Coastal and Marine Science Center, U.S. Geological Survey, 2885 Mission Street, Santa Cruz, California 95060, USA
[2]Geological Survey of Canada (Pacific), 9860 West Saanich Road, Sidney, British Columbia V8L 4B2, Canada
[3]Woods Hole Coastal and Marine Science Center, U.S. Geological Survey, 384 Woods Hole Road, Woods Hole, Massachusetts 02543, USA
[4]Department of Geoscience, University of Calgary, 2500S University Drive NW, Calgary, Alberta T2N 1N4, Canada
[5]Moss Landing Marine Laboratories and Tombolo Mapping Laboratory, San Jose State University, 8272 Moss Landing Road, Moss Landing, California 95039, USA
[6]Geochronology and Tracers Facility, British Geological Survey, Keyworth, Nottingham NG12 5GG, UK

## ABSTRACT

**Fluid seepage along obliquely deforming plate boundaries can be an important indicator of crustal permeability and influence on fault-zone mechanics and hydrocarbon migration. The ~850-km-long Queen Charlotte fault (QCF) is the dominant structure along the right-lateral transform boundary that separates the Pacific and North American tectonic plates offshore southeastern Alaska (USA) and western British Columbia (Canada). Indications for fluid seepage along the QCF margin include gas bubbles originating from the seafloor and imaged in the water column, chemosynthetic communities, precipitates of authigenic carbonates, mud volcanoes, and changes in the acoustic character of seismic reflection data. Cold seeps sampled in this study preferentially occur along the crests of ridgelines associated with uplift and folding and between submarine canyons that incise the continental slope strata. With carbonate stable carbon isotope ($\delta^{13}C$) values ranging from –46‰ to –3‰, there is evidence of both microbial and thermal degradation of organic matter of continental-margin sediments along the QCF. Both active and dormant venting on ridge crests indicate that the development of anticlines is a key feature along the QCF that facilitates both trapping and focused fluid flow. Geochemical analyses of methane-derived authigenic carbonates are evidence of fluid seepage along the QCF since the Last Glacial Maximum. These cold seeps sustain vibrant chemosynthetic communities such as clams and bacterial mats, providing further evidence of venting of reduced chemical fluids such as methane and sulfide along the QCF.**

Nancy G. Prouty https://orcid.org/0000-0002-8922-0688

## INTRODUCTION

Fluids play an important role along plate boundaries because they influence almost every chemical, physical, mechanical, and thermal process that occurs in the lithosphere (Judd and Hovland, 2007; Kastner et al., 1991; Saffer and Tobin, 2011; Tryon et al., 2001). Such processes are all directly impacted by the transport of mass, heat, and chemical species in a hydrogeologic framework (Tryon et al., 2001). In turn, these processes can influence fluid and gas budgets and geochemical cycling (Kopf, 2002) as well as support chemosynthetic communities on the seafloor (e.g., Levin et al., 2016). Fluid seepage by cold seeps, where hydrogen sulfide, methane, and other hydrocarbon-rich fluids are released into the sediment and water column, plays an important role in transferring methane carbon from storage in ocean-floor sediments into the ocean and atmosphere. For example, Judd (2004) estimated that global methane fluxes from the seafloor to the ocean and atmosphere vary between 0.4 and 48 Tg/yr. In contrast to hydrothermal vents, temperatures of cold seeps (referred to herein as seeps) are similar to surrounding seawater temperatures. Some mechanisms of fluid seepage at seeps include fluid flow driven by excess pore pressure in areas of high sedimentation (Berndt, 2005), seismic activity (e.g., Fischer et al., 2013), links to sea-level lowstands (Feng et al., 2010; Liebetrau et al., 2010; Teichert et al., 2003), hydrological and tidal pumping, and warming of bottom water (Suess, 2014). These temporally recent processes are superimposed on geologic controls of fluid migration, whereby the geologic setting defines seep characteristics and the driving mechanisms of fluid expulsion (Judd and Hovland, 2007; Suess, 2014). For example, rapid sediment loading along passive margins promotes seep development due to pore fluid overpressure (Dugan and Flemings, 2002), and at active convergent margins, plate motions facilitate faulting and deformation, leading to sediment compaction, the formation of fluid pathways, and traps for deeply sourced fluids that control seepage patterns (Kluesner et al., 2013; Sahling et al., 2008; Watson et al., 2019). Seeps documented along strike-slip fault systems are most commonly observed along zones of transpression and folding (Dupré et al., 2015; Fossen et al., 2010; Kluesner and Brothers, 2016; Paull et al., 2008). For example, recent investigations along the strike-slip margin in southern and central California (USA) suggest that localized areas of transpression along transform faults may generate tectonic features such as fault bends and stepovers, which appear to act as loci of substrate fluid flow (Kluesner and



Downloaded from http://pubs.geoscienceworld.org/gsa/geosphere/article-pdf/16/6/1336/5182833/1336.pdf
by MBL WHOI Library user

Brothers, 2016) and in turn support chemosynthetic habitats and authigenic carbonate formation (Conrad et al., 2018; Maloney et al., 2015; Stakes et al., 1999). Similar patterns have been observed in the Sea of Marmara (Turkey), where seeps are preferentially clustered along zones of localized uplift, folding, and transpressional bending along the North Anatolian fault (Dupré et al., 2015), as well as along the Mendocino transform fault (offshore California; Stakes et al., 2002) and Guaymas Basin (offshore Mexico; Hensen et al., 2019; Paull et al., 2007), where active seafloor fluid seepage along transform margins may represent important conduits for facilitating vertical fluid flow.

Authigenic carbonates commonly form at seeps as a result of anaerobic oxidation of methane (AOM) via sulfate reduction ($CH_4 + SO_4^{2-} \rightarrow HCO_3^- + HS^- + H_2O$). The production of bicarbonate ($HCO_3^-$) increases the pore-fluid alkalinity and favors carbonate precipitation. These carbonates represent a proxy record of the local and regional controls on the source and flux of methane carbon, the conditions and environment under which carbonates formed, and information regarding fluid-sediment and fluid-rock interactions (Campbell, 2006; Formolo et al., 2004; Magalhães et al., 2012; Naehr et al., 2007). For example, differences in the isotopic composition of carbonate cements along the Cascadia margin (northeastern Pacific) highlight the contrasting hydrogeologic settings between shallow-sourced fluids in a thrust-fault setting versus a deep origin of fluids from a strike-slip fault associated with an accretionary wedge (Sample and Reid, 1998). Integrating geochemistry, mineralogy, and petrology of authigenic carbonates with multichannel seismic reflection (MCS) profiles as well as multibeam bathymetry, backscatter, and water-column imaging data offers a valuable opportunity to investigate the relationship between fluid flow, sedimentation patterns, and tectonics along a proglacial transform margin. To evaluate potential flow pathways and sources of fluid flow along the Queen Charlotte fault (QCF; offshore southeastern Alaska [USA] and western British Columbia [Canada]), a series of authigenic carbonates was collected and analyzed in a collaborative research program between the U.S. Geological Survey (USGS) and the Geological Survey of Canada. Data collected between 2009 and 2018 included geophysical surveys (multibeam bathymetric imaging, backscatter, multichannel seismic reflection profiling, and 3.5 kHz CHIRP subbottom profiling), piston coring, seafloor photography, grab sampling, and conductivity-temperature-depth (CTD) casts along the continental margin of western British Columbia and southeastern Alaska (Barrie et al., 2013, 2018; Brothers et al., 2019; Greene et al., 2019). This paper presents the first comprehensive examination of seabed fluid-flow indicators along the QCF margin, including gas bubbles observed in water-column backscatter data, the presence of chemosynthetic communities such as bacterial mats and bivalves, precipitates of authigenic carbonate rocks and pavement, and mud volcanoes (Barrie et al., 2020). We also evaluate structural and stratigraphic controls on fluid-flow pathways using seismic reflection profiles. Results from this study therefore expand our understanding of the possible origin and occurrence of fluid seepage along an ocean-continent transform boundary and test the assumption that seeps along strike-slip fault systems are focused along faults and zones of transpressional folding in a poorly studied geographic region.

The offshore QCF and its northern onshore extension, the Fairweather fault, form an ~1150-km-long transform boundary that separates the Pacific and North American tectonic plates (Fig. 1). Early studies noted evidence for progressive right-lateral offset on the QCF at the southern edge of the Yakobi Sea Valley (Fig. 1) and mapped its general location along the ocean-continent boundary for another ~800 km southward to the Queen Charlotte triple junction (Bruns and Carlson, 1987; Hyndman and Hamilton, 1993; Rohr and Furlong, 1996; Von Huene et al., 1979). While the QCF carries ~50 mm/yr of right-lateral transform motion, portions of the plate boundary are also transpressive (Brothers et al., 2020; Hyndman and Hamilton, 1993; Rohr et al., 2000; Tréhu et al., 2004). Convergence rates are expected to increase gradually southward from the Yakobi Sea Valley, where the QCF is closely aligned with plate motion, to a maximum near the southern end of the fault and west of Haida Gwaii (British Columbia; Fig. 1; Brothers et al., 2019, 2020; Hyndman, 2015; Rohr et al., 2000; Tréhu et al., 2015). The oblique convergence expected to the west of Haida Gwaii has led to the buildup of the Queen Charlotte terrace, a ~25-km-wide, ~150-km-long topographic platform located between the QCF on the east and the abyssal ocean basin to the west (Fig. 1). Within this region, local transpressional bends along the fault may generate even higher rates of convergence (as much as 15–20 mm/yr), which is evident in the tectonic geomorphology observed along the southern QCF (Brothers et al., 2020). The formation of the terrace has been described by competing end-member models: one attributes the terrace to an accreted sediment wedge from oblique subduction of the Pacific plate beneath Haida Gwaii (e.g., Hyndman, 2015; Hyndman and Hamilton, 1993), the other to transpressional deformation and crustal thickening of the eastern edge of the Pacific plate (Brothers et al., 2020; Rohr et al., 2000; Tréhu et al., 2015). Although these competing models are expected to generate distinct differences in crustal fluid flow and deformation patterns, the terrace contains relatively sparse geophysical observations. South of Haida Gwaii, plate-boundary deformation becomes distributed (e.g., Rohr, 2015; Rohr and Furlong, 1996), but the transform boundary ultimately links with Explorer Ridge, where nascent oceanic crust is translated to the northwest along the QCF (Rohr et al., 2000).

A series of recent earthquakes generated substantial interest in the QCF margin beginning with a M7.8 thrust event near Haida Gwaii in 2012 and followed by a M7.5 strike-slip event west of Craig (Alaska) in 2013 (Brothers et al., 2017; Lay et al., 2013; Yue et al., 2013). However, at the time of the 2012 event, the morphology of the QCF and surrounding continental slope within U.S. waters had not been comprehensively surveyed using high-resolution multibeam sonar or modern seismic reflection profiling techniques, and only a narrow strip of seafloor along the QCF had been mapped this way in Canadian waters (Barrie et al., 2013). Therefore, detailed information about the physical properties of the offshore margin was sparse, and little evidence for fluid seepage had been directly documented. Furthermore, recently documented


Downloaded from http://pubs.geoscienceworld.org/gsa/geosphere/article-pdf/16/6/1336/5182833/1336.pdf
by MBL WHOI Library user

submarine landslides along the margin attest to the potential for earthquake triggering of slope failures (Brothers et al., 2019; Greene et al., 2019). Taken together, high rates of sediment accumulation, fluid overpressure from sediment compaction, and tectonic deformation can generate a variety of sources for focused fluid flow and seafloor seeps. An active seafloor seep was discovered in 2011 offshore Haida Gwaii (Barrie et al., 2013) and another in 2015 along the crest of a ridge located near the international border (Greene et al., 2019). Greene et al. (2019) proposed that fluid flow is prominent along most of the central and southern QCF and that fluid flow indicators occur close to, or within, the fault zone, which in turn may be acting as a conduit for the venting of gases and fluids. In addition, the gas could be accumulating in antiforms that form many of the conjugate ridges described by Tréhu et al. (2015) along the continental slope. Gas plumes could originate from multiple sources, such as from the compaction and degradation of organic-rich sediment, continuously forming hydrocarbon reservoirs (Tinivella and Giustiniani, 2012), and dissolution of clathrates or frozen gas-hydrate systems (Depreiter et al., 2005; Dickens and Quinby-Hunt, 1994; Dimitrov, 2002; Sauter et al., 2006; Tinivella and Giustiniani, 2012).

## MATERIAL AND METHODS

### Geophysical Data

Seafloor mapping and morphological analyses presented in this study are based on several multibeam echosounder (MBES) data sets. The QCF and surrounding slope were mapped between 2009 and 2018 using high-resolution MBES systems, including a Reson Seabat 7160 (44 kHz) aboard the R/V *Medeia*, a Reson Seabat 7111 (100 kHz) aboard the R/V *Solstice*, and a Kongsberg Simrad EM710 (70 kHz) aboard the U.S. National Oceanic and Atmospheric Administration (NOAA) Ship *Fairweather* and the Canadian Coast Guard Ship (CCGS) *Vector* (Balster-Gee et al., 2017a; Barrie et al., 2018; Brothers et al., 2019; Greene et al., 2019). These data were merged with lower-resolution multibeam

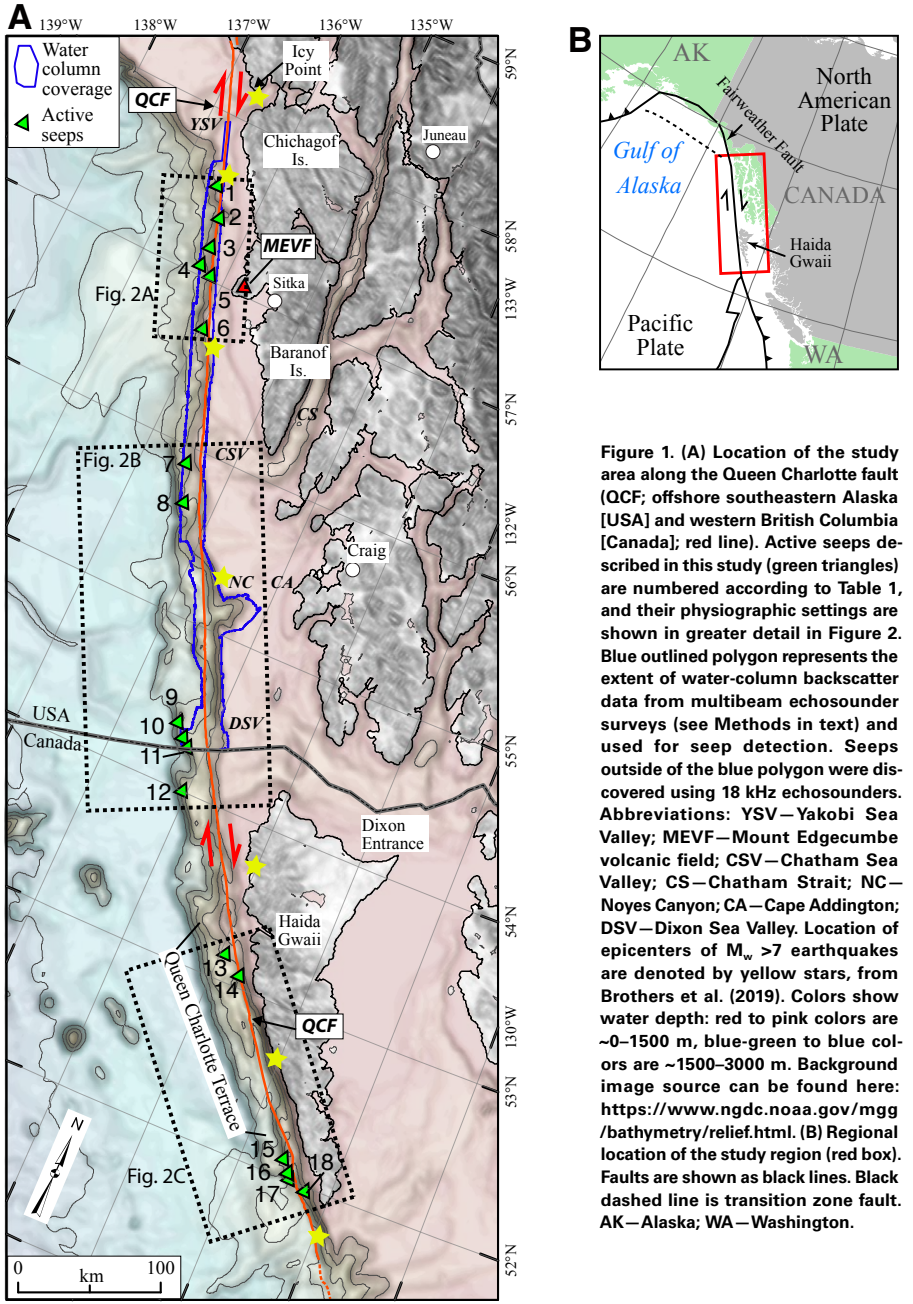


**Figure 1. (A) Location of the study area along the Queen Charlotte fault (QCF; offshore southeastern Alaska [USA] and western British Columbia [Canada]; red line). Active seeps described in this study (green triangles) are numbered according to Table 1, and their physiographic settings are shown in greater detail in Figure 2. Blue outlined polygon represents the extent of water-column backscatter data from multibeam echosounder surveys (see Methods in text) and used for seep detection. Seeps outside of the blue polygon were discovered using 18 kHz echosounders. Abbreviations: YSV—Yakobi Sea Valley; MEVF—Mount Edgecumbe volcanic field; CSV—Chatham Sea Valley; CS—Chatham Strait; NC—Noyes Canyon; CA—Cape Addington; DSV—Dixon Sea Valley. Location of epicenters of $M_w$ >7 earthquakes are denoted by yellow stars, from Brothers et al. (2019). Colors show water depth: red to pink colors are ~0–1500 m, blue-green to blue colors are ~1500–3000 m. Background image source can be found here: https://www.ngdc.noaa.gov/mgg/bathymetry/relief.html. (B) Regional location of the study region (red box). Faults are shown as black lines. Black dashed line is transition zone fault. AK—Alaska; WA—Washington.**


Downloaded from http://pubs.geoscienceworld.org/gsa/geosphere/article-pdf/16/6/1336/5182833/1336.pdf
by MBL WHOI Library user

bathymetry data sets and coastal relief models spanning the Gulf of Alaska region (available at https://www.ngdc.noaa.gov/mgg/bathymetry/relief.html). Bathymetry data were processed using the Teledyne CARIS HIPS software package and included offset corrections, tidal corrections, sound velocity correction, ping editing, and gridding. Raster surface derivatives (hillshade, gradient, and aspect) for the high-resolution data were created from 20 m bathymetric elevation models and used to interpret seabed morphology along the entire length of the QCF (Brothers et al., 2020). The MBES surveys along the continental slope in U.S. waters recorded water-column backscatter data (blue polygon on Fig. 1A), and bubble plumes were detected using the *FM Midwater* module within the QPS Fledermaus software package. Mapped bubble plumes were then combined with multibeam bathymetry and seismic reflection profiles for visualization and interpretation. MBES water-column data were not recorded during surveys in Canadian waters. However, single-beam 18 kHz profiles were collected using a Simrad EK60 onboard the R/V *Ocean Starr* in 2017 and the CCGS *John P. Tully* in 2011, 2015, and 2017, leading to discoveries of several bubble plumes in the water column. Although some seafloor ridges were suspected to be sites of seepage and so were specifically targeted for survey by EK60, we consider the southern half of the margin to be less thoroughly surveyed for seeps than areas to the north.

High-resolution multichannel seismic data were also collected in conjunction with bathymetry data onboard the R/V *Medeia* in the spring of 2016 (Balster-Gee et al., 2017a). The seismic shots were generated using a SIG 2Mille 50-tip mini-sparker operated at 1200 J. Reflected arrivals were recorded using a 32-channel solid-core, digital GeoEel streamer system. Additional MCS data were collected in 2016 onboard the R/V *Norseman* using an Applied Acoustic Delta Sparker Sled operated at 2400 J and a 64-channel GeoEel streamer system (Balster-Gee et al., 2017b). Recorded SEGD shots (SEGD file format is one of several standards developed by the Society of Exploration Geophysicists for storing geophysical data) were processed using the academic software packages SIOSEIS and Seismic Unix, as well the commercial Paradigm Echos software package. Seismic processing largely followed the approach described by Kluesner et al. (2018). After processing, seismic imagery was merged with multibeam bathymetry and mapped water-column gas plumes using the QPS Fledermaus software package.

Seismic attribute calculations can provide quantitative justification for the interpretation of a particular geologic feature. A powerful approach to detect geologic targets and isolate their acoustic response involves the combination of multiple attributes with structurally orientated calculations and discontinuity-attribute calculations (e.g., Gersztenkorn and Marfurt, 1999; Kluesner and Brothers, 2016; Marfurt et al., 1999; Tingdahl and de Groot, 2003; Tingdahl et al., 2001). This study applied a fully connected multilayer perceptron neural-network approach to two-dimensional high-resolution MCS profiles to optimize the detection of gas and fluid migration pathways in the vicinity of active seep sites (Brothers et al., 2014; Connolly, 2015; Heggland, 2005; Kluesner et al., 2013; Ligtenberg, 2005). Within the OpendTect software package, 36 attributes were used as input nodes into the supervised neural-network chimney calculation, and each node was weighted during the neural-network training (for details, see Table S1 in the Supplemental Material[1]; Kluesner and Brothers, 2016; Brothers et al., 2014). The single hidden layer of the neural network consists of 15 nodes, and training was stopped when the normalized root-mean-square (RMS) error of the training set, as well as the misclassification percentage, reached a minimum value. Training was stopped before the RMS error trend shifted upward to prevent overfitting of the data and overtraining of the neural net. The generated meta-attribute represents a measurement of probability for the presence of a chimney structure, with 0 representing the lowest probability and 1 representing the highest. The chimney meta-attribute results were projected onto seismic cross-sections using a gradational color scale that reveals only the highest (~80% and above) chimney probabilities. The chimney analysis was used to identify two features: zones of probable fluid migration (e.g., vertical pipes, faults, and chimneys) and gassy sediments. The frequency-dependent reflectivity of gassy sediments due to scattering and absorption has been previously documented (e.g., Wood et al., 2008). The chimney meta-attribute analysis described above therefore represents a powerful method to discern subtle patterns of gas-related attenuation and their spatial relationships with the surrounding structure and stratigraphy.

## Geologic Sample Collection

Seep sites (seeps 1–18; Fig. 1A) identified in acoustic data were targeted for carbonate and sediment sampling during three cruises on the CCGS *John P. Tully* in 2011, 2015, and 2017 and are assigned station numbers in Table 1 (e.g., 2017-STN15). Given weather and time restraints, 11 authigenic carbonate samples were collected at seven of the 18 seep sites. Authigenic carbonate samples were collected at water depths ranging from 507 to 1003 m, either by a grab sampler developed by Institutt for Kontinentalsokkelundersøkelser (Trondheim, Norway), capable of collecting a 1 $m^3$ sample of relatively undisturbed sediment or rock, or from a piston corer (Table 1). In the northern QCF region, a large carbonate sample (2017-STN15) was collected in 2017 on a seep site (seep 3; Table 1) situated on a bathymetric ridge where a gas plume was present, extending 250 m from the seafloor in height (Figs. S3A, S3B [footnote 1]). Within the central QCF region, two authigenic carbonate samples were collected in 2017 (2017-STN40 and 2017-STN41) at an active seep site (seep 8; Table 1; Figs. S8A, S8B) near the mouth of the Chatham Sea Valley (Alaska), and one was collected at the active Chatham Fan gas seep site (seep 7; 2017-STN04; Table 1; Figs. S7A, S7B). Based on in situ photographs, bacterial mats and bivalve shells were also observed in this region. Farther south in the central QCF region, three carbonate samples (2015-STN34, 2015-STN35, and 2017-STN03) were collected in 2015 and 2017 in the vicinity of the mud volcano identified by Barrie et al. (2020) west of the Dixon Sea Valley (seep 11; Figs. 1, 2B), where a plume was detected in the 18 kHz data and previously detected extending 700 m into the water column in 2015 and 350 m in 2017 (Barrie et al.,

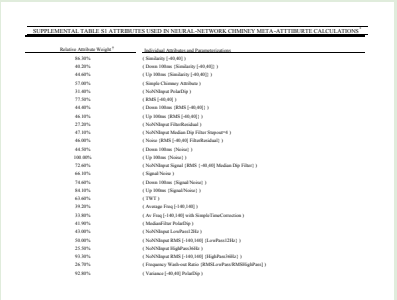

SUPPLEMENTAL TABLE S1 ATTRIBUTES USED IN NEURAL-NETWORK CHIMNEY META-ATTTRIBUTE CALCULATIONS

| Relative Attribute Weight[1] | Individual Attributes and Parameterizations |
|---|---|
| 86.30% | ( Similarity [-40,40] ) |
| 40.20% | ( Dome 100ms [Similarity [-40,40]] ) |
| 64.60% | ( Up 300ms [Similarity [-40,40]] ) |
| 57.00% | ( Simple Chimney Attribute ) |
| 31.40% | ( NoNNInput PolarDip ) |
| 77.30% | ( RMS [-40,40] ) |
| 44.40% | ( Dome 100ms [RMS [-40,40]] ) |
| 66.10% | ( Up 300ms [RMS [-40,40]] ) |
| 27.20% | ( NoNNInput FilterResidual ) |
| 87.10% | ( NoNNInput Median Dip Filter Stepout=6 ) |
| 46.00% | ( Noise [RMS [-40,40] FilterResidual] ) |
| 44.50% | ( Dome 100ms [Noise] ) |
| 100.00% | ( Up 300ms [Noise] ) |
| 72.60% | ( NoNNInput Signal [RMS [-40,40] Median Dip Filter] ) |
| 64.10% | ( Signal/Noise ) |
| 74.60% | ( Dome 100ms [Signal/Noise] ) |
| 84.10% | ( Up 300ms [Signal/Noise] ) |
| 63.60% | ( TWT ) |
| 39.20% | ( Average Freq [-40,140] ) |
| 33.80% | ( Av Freq [-40,140] with SimpleTimeCorrection ) |
| 41.90% | ( Median Filter PolarDip ) |
| 63.00% | ( NoNNInput LowPass120z ) |
| 50.00% | ( NoNNInput RMS [-160,160] [LowPass120z] ) |
| 25.50% | ( NoNNInput HighPass360z ) |
| 93.30% | ( NoNNInput RMS [-160,160] [HighPass360z] ) |
| 26.70% | ( Frequency Wash-out Ratio [RMSLowPassRMSHighPass] ) |
| 92.00% | ( Variance [-40,40] PolarDip ) |

[1]Supplemental Material. Contains additional information on neural-network chimney meta-attribute analysis, U-Th analysis as well as additional figures for water column data, multichannel seismic reflection profile, and multibeam echosounder (MBES) data. Please visit https://doi.org/10.1130/GEOS.S.12986090 to access the supplemental material, and contact editing@geosociety.org with any questions.



Downloaded from http://pubs.geoscienceworld.org/gsa/geosphere/article-pdf/16/6/1336/5182833/1336.pdf
by MBL WHOI Library user

TABLE 1. SUMMARY OF DETECTED SEEP SITES AND SAMPLE STATIONS

| Seep | Sample station | Latitude (°N) | Longitude (°W) | Water depth (m) | Plume height (m) | Detection method | Sample method | Date of collection | Site description | Supplemental figure(s) |
|---|---|---|---|---|---|---|---|---|---|---|
| 1 | N.A.* | 57.574 | 136.548 | 198 | 125 | MBES | N.A. | N.A. | Interfluvial ridge | S1 |
| 2 | N.A. | 57.389 | 136.357 | 192 | 90 | MBES | N.A. | N.A. | Shelf | S2 |
| 3 | 2017-STN15 | 57.200 | 136.308 | 507 | 300 | MBES | Grab sample | 19 Sep 2017 | Interfluvial ridge | S3A, S3B |
| 4 | N.A. | 57.076 | 136.322 | 924 | 500 | MBES | N.A. | N.A. | Interfluvial ridge | S4 |
| 5 | 2017-STN37 | 57.038 | 136.165 | 596 | 380 | MBES | N.A. | N.A. | Fault | S5A, S5B |
| 6 | N.A. | 56.720 | 135.979 | 272 | 150 | MBES | N.A. | N.A. | Shelf ridge | S6 |
| 7 | 2017-STN04 | 55.910 | 135.499 | 714 | 600 | MBES | Piston core | 18 Sep 2017 | Anticlinal ridge | S7A, S7B |
| 8 | 2017-STN40 | 55.678 | 135.341 | 631 | 330 | MBES | Grab sample | 23 Sep 2017 | Anticlinal ridge | S8A, S8B |
| | 2017-STN41 | 55.680 | 135.337 | 627 | | | Grab sample | 23 Sep 2017 | | |
| 9 | N.A. | 54.404 | 134.394 | 885 | 500 | EK60 | N.A. | N.A. | Anticlinal ridge | S9 |
| 10 | N.A. | 54.327 | 134.277 | 1501 | N.D.# | MBES | N.A. | N.A. | Anticlinal ridge | N.A. |
| 11 | 2017-STN03 | 54.279 | 134.192 | 982 | 700†, 350§ | EK60 | Piston core | 17 Sep 2017 | Anticlinal ridge | S11A, S11B |
| | 2015-STN34 | 54.279 | 134.195 | 1003 | | | Grab sample | 24 Sep 2015 | | |
| | 2015-STN35 | 54.279 | 134.195 | 1002 | | | Grab sample | 24 Sep 2015 | | |
| 12 | 2017-STN56 | 54.018 | 134.048 | 900 | N.D. | EK60 | N.A. | N.A. | Anticlinal ridge | N.A. |
| 13 | N.A. | 53.181 | 132.947 | 740 | 250 | EK60 | N.A. | N.A. | Landslide | S13 |
| 14 | N.A. | 53.090 | 132.722 | 810 | 370 | EK60 | N.A. | N.A. | Fault | S14 |
| 15 | N.A. | 52.130 | 131.577 | 563 | N.D. | EK60 | N.A. | N.A. | Cone (guyot) | N.A. |
| 16 | 2011-STN43 | 52.057 | 131.485 | 796 | 250 | EK60 | Grab sample | 7 Jul 2011 | Cone | S16 |
| 17 | 2017-STN65 | 52.018 | 131.451 | 802 | N.D. | EK60 | Grab sample | 28 Sep 2017 | Cone | N.A. |
| 18 | N.A. | 51.987 | 131.254 | 335 | 335 | EK60 | N.A. | N.A. | Ridge | N.A. |

*Note*: Plumes were detected in the water column using two different methods: (1) MBES refers to multibeam echosounder and (2) EK60 is an echo sounder. See text footnote 1 for supplemental figures.
*N.A.—refers to a seep location but where no station was conducted for sampling.
†Apparent height in EK60 data collected in 2015.
§Apparent height in EK60 data collected in 2017.
#N.D.—not determined.

2020; Figs. S11A, S11B, S18). Two additional carbonate samples (2017-STN65 and 2011-STN43) were collected from the southern QCF region located near Haida Gwaii, south of the Queen Charlotte terrace and between the Dellwood fault and the QCF (Fig. 1) at seeps 17 and 16, respectively (Fig. S16). Based on in situ photographs, these sites are characterized by carbonates, lithified mudstone, gravel, and clam beds. Sediment recovered from a piston core suggests a mixture of grain sizes from clay to gravel and igneous material, including angular granitic or granodiorite clasts.

## Geochemical Analysis

### *X-Ray Diffraction and Petrography*

Thin sections were investigated microscopically for textural, compositional, and morphological features of carbonate precipitation. Mineralogy was determined by X-ray diffraction (XRD) using a Philips XRD with graphite monochromator at 40 kV and 45 mA as described in Prouty et al. (2016). Step scans were run from 5° to 65° 2θ with 0.02° steps, using CuKα radiation and a count time of 2 s per step following Hein et al. (2013). XRD digital scan data were analyzed using the Philips X'Pert HighScore search-and-match function to identify minerals. The XRD 100 intensity peak at 2θ for calcite was 29.4 degrees; dolomite, 30.8 degrees; quartz, 26.6 degrees; and aragonite, 26.2 degrees. Relative contributions (relative percentage of carbonate minerals within each sample) are reported as major (>25%), moderate (5%–25%), and minor (<5%). Calcium carbonate content, reported as weight percent (wt%), was determined using a coulometer at the USGS Pacific Coastal and Marine Science Center (Santa Cruz, California).


Downloaded from http://pubs.geoscienceworld.org/gsa/geosphere/article-pdf/16/6/1336/5182833/1336.pdf
by MBL WHOI Library user

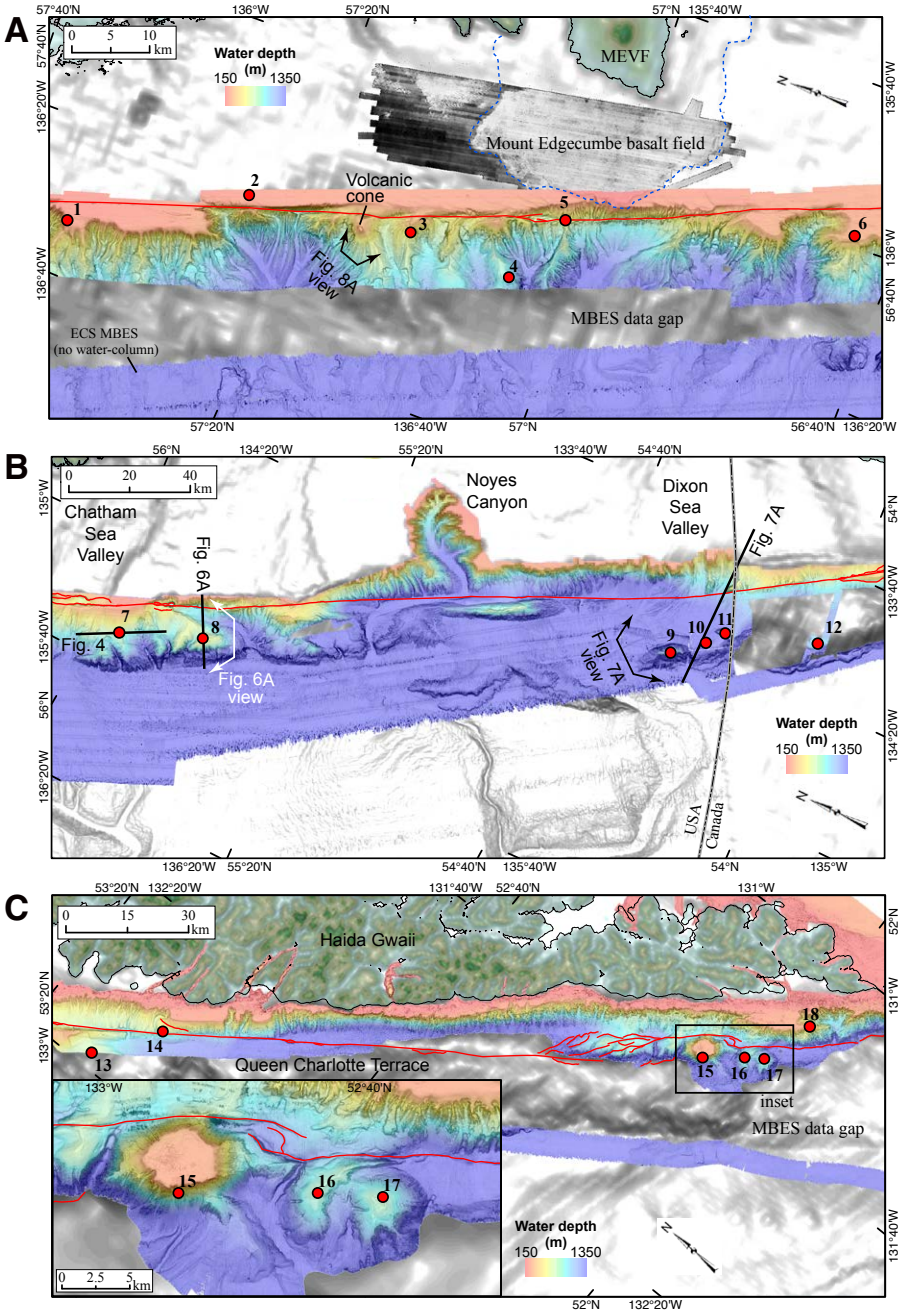


**Figure 2. Shaded-relief imagery surrounding seep sites along the Queen Charlotte fault (red lines) for the northern section from the Yakobi Sea Valley to the Chatham Sea Valley (A), the central section from Chatham Sea Valley to the Dixon Sea Valley (to the USA-Canada border) (B), and the southern section from the Dixon Sea Valley to the southern end of Haida Gwaii (C). Active seeps (red circles) described in this study are numbered according to Table 1. Gray regions represent areas that do not contain high-resolution multibeam bathymetry data, including the Mount Edgecumbe basalt field that extends to the shelf edge (Greene et al., 2007). High backscatter is represented by white, and low backscatter is represented by black. See Figure 1 for panel locations, and Table 1 for detailed information on seep sites. MEVF—Mount Edgecumbe volcanic field; ECS—extended continental shelf; MBES—multibeam echosounder. Shaded-relief data/imagery from https://www.ngdc.noaa.gov/mgg/bathymetry/relief.html.**

### *Stable Isotopes*

A handheld pneumatic drill (Dremel) was used to sample various components of the authigenic carbonates. The resulting powdered carbonate was collected and analyzed for stable carbon ($\delta^{13}C$) and oxygen ($\delta^{18}O$) isotopic composition using a ThermoScientific Kiel IV carbonate device interfaced to a ThermoScientific MAT-253 dual-inlet isotope ratio mass spectrometer at the University of California, Santa Cruz (UCSC) Stable Isotope Laboratory. Stable isotope values are reported in per mil (‰) relative to the international reference Vienna Peedee belemnite. Analytical uncertainties (1σ) are 0.05‰ for $\delta^{13}C$ and 0.10‰ for $\delta^{18}O$.

Subsamples from the authigenic carbonate samples were analyzed for radiogenic strontium isotope ($^{87}Sr/^{86}Sr$) composition. In brief, using an agate mortar and pestle, the carbonate was homogenized, and dissolved in 2 N $HNO_3$ and filtered to minimize contamination from associated insoluble fractions (e.g., clays and other silicates) entrained in the carbonate. Samples were digested in sealed Teflon vessels following the protocol from Bullen et al. (1996), whereby Sr was separated from other ions using a Bio-Rad AG-502-X8 cation exchange resin with HCl as the eluent. The purified Sr was then converted to nitrate form, taken up in 30 μL


Downloaded from http://pubs.geoscienceworld.org/gsa/geosphere/article-pdf/16/6/1336/5182833/1336.pdf
by MBL WHOI Library user

of 0.15 M $H_3PO_4$, and loaded onto a Ta ribbon. The isotopic composition was measured on a Finnigan MAT 261 multicollector mass spectrometer using a static collection mode at the USGS facility at Menlo Park, California (Bullen et al., 1996). The $^{87}Sr/^{86}Sr$ values have been corrected for analytical fractionation to the standard $^{88}Sr/^{86}Sr$ ratio of 8.37521, and measurements are precise to ±0.00002 at the 95% confidence level.

### Uranium-Thorium Dating

Dating of select authigenic carbonates was conducted at the British Geological Survey Natural Environment Research Council (NERC) Geochronology and Tracers Facility (Keyworth, UK) using an analytical protocol outlined in Prouty et al. (2016) and modified from Edwards et al. (1987) and Shen et al. (2002). Powdered carbonate samples were processed via total dissolution techniques, with isotope ratios measured on a Thermo Neptune Plus multicollector inductively coupled plasma mass spectrometer (ICP-MS) relative to a mixed $^{229}Th$-$^{236}U$ tracer calibrated against gravimetric solutions of CRM 112a uranium reference material and Ames Laboratory high-purity Th. The authigenic carbonates can incorporate detrital material that carries $^{232}Th$ and an associated amount of initial $^{230}Th$ that is not related to the in situ decay of $^{234}U$. Therefore, a correction is required to calculate a reliable carbonate precipitation age. In lieu of site-specific detrital isotopic composition (e.g., Bayon et al., 2015; Teichert et al., 2003), the detrital isotopic composition was based on measured sediment values from Prouty et al. (2016) from 385 and ~1600 m below sea level along the U.S. Atlantic margin, with the detrital $^{230}Th/^{238}U$ value for each sample or site interpolated based on water depth. This correction accounts for both the $^{230}Th$ contained within the detrital grains themselves and the so-called hydrogenous $^{230}Th$ produced by the decay of U dissolved in the water column, which is adsorbed onto the surfaces of sediment particles. Using the decay constants of Cheng et al. (2013), U-Th age calculations were performed using an in-house Microsoft Excel spreadsheet.

### Gases

The void gas from sample 2017-STN03 at seep 11 was sampled directly from gas trapped in the core liner at 160 cm downcore using a gas-tight syringe, and injected into an evacuated 30 ml serum vial equipped with septa for geochemical analysis, thereby keeping it sealed from mixing with ambient air. Sediment collected for headspace gas analyses was sampled between 205 and 215 cm downcore and was collected by placing a 10 cm section of core from the core cutter into a septa-equipped 1 L sample can. Seawater was added to the brim of the can, and then 200 ml of this water was removed to create a 200 ml headspace. The can was sealed and shaken for 5 min. In preparation for geochemical analysis, gas was extracted using a syringe. Both void gas and headspace gases were analyzed by gas chromatography following the methods of Kvenvolden (1993) at the USGS Pacific Coastal and Marine Science Center. Gas samples collected directly as gas (void gas) and as sediment gas are reported in parts per million by volume (ppm); methane ($C_1$), ethane ($C_2$), propane ($C_3$), isobutane ($iC_4$), normal butane ($nC_4$), isopentane ($iC_5$), and normal pentane ($nC_5$). Methane carbon isotopic composition was performed on a laser-based Los Gatos Research methane isotope analyzer (DLT-100). Samples were injected into a known-volume cell where the length of the laser path is determined as a function of the carbon isotope. The results are reported as per mil (‰) relative to Vienna Peedee belemnite. The accuracy of the measurements is ±0.5‰.

## RESULTS

### Seep Identification, Distribution, and Characteristics

A total of 18 active seeps were discovered in this study based on detection of bubble plumes in the water column (Fig. 1; Table 1). Backscatter anomalies were not observed at active seep sites or at sites where authigenic carbonates were collected. Instead, in areas of rugged topography along the continental slope, backscatter anomalies were observed presumably due to changes in sediment lithology such as grain size and sand content in and around channels, galleys, and submarine canyons. In this section, seep distribution is described in terms of the seafloor geomorphology and substrate characteristics along distinct kinematic sections of the QCF (following Brothers et al., 2020). The northern section extends from the Yakobi Sea Valley to the Chatham Sea Valley, the central section from the Chatham Sea Valley to the Dixon Sea Valley (to the USA-Canada border), and the southern section from the Dixon Sea Valley to the southern end of Haida Gwaii (Fig. 1).

Six seeps were identified along the northern section of the QCF and to the west of Baranof and Chichagof Islands (Figs. 1A, 2A). The QCF in this region crosses the upper slope and outer shelf, and deformation appears to be concentrated within a narrow zone along the seafloor fault trace (Brothers et al., 2019, 2020). The continental slope to the west of the QCF is characterized by networks of submarine canyons and submarine landslide scars but displays little or no evidence of active tectonic deformation away from the mapped trace of the QCF. Seeps 1, 2, and 6 are located along the shelf edge at distances of 1.5–3.7 km away from the QCF, seeps 3 and 4 are located near the crests of ridges that separate submarine canyons or gullies, and seep 5 appears to be on the QCF (Fig. 2A). MCS profiles crossing the canyonized morphology (e.g., Fig. 3) reveal stratigraphic layering beneath the ridgelines that has been disrupted and show bottom-simulating reduction in acoustic frequency and amplitude, or acoustic wipeout, that we infer to be associated with sediments containing free gas trapped below the base of the gas hydrate stability zone (GHSZ) (Chand and Minshull, 2003). The bottom-simulating change in character, which is most evident in the chimney meta-attribute calculation, cross-cuts reflectors under the ridgelines to either side of seep 4 but is not evident directly below the seep site. A narrow zone of vertically disrupted strata, or pipe (Fig. 3B inset), extends vertically above a cone of acoustic wipeout beneath the ridgeline.

Six seeps were identified along the central section of the QCF (Fig. 2B). The continental slope


Downloaded from http://pubs.geoscienceworld.org/gsa/geosphere/article-pdf/16/6/1336/5182833/1336.pdf
by MBL WHOI Library user

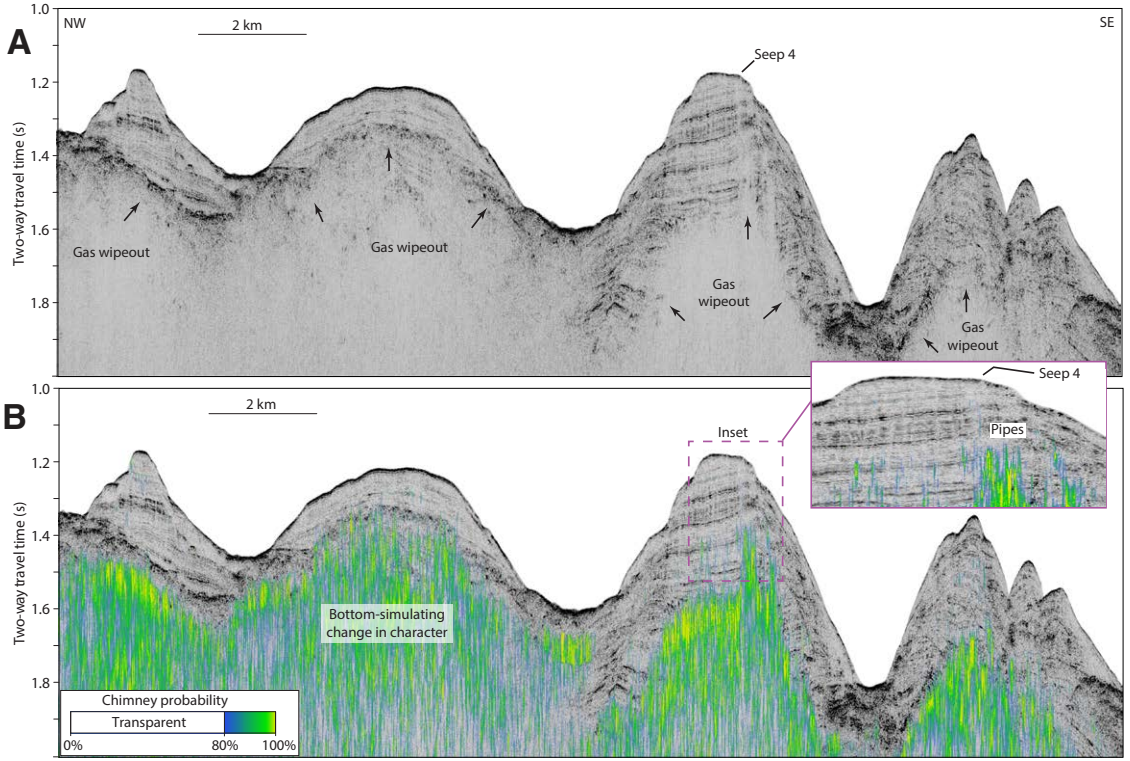


**Figure 3. (A) Multichannel seismic reflection profile (see Fig. 2A for location) crossing a series of intercanyon ridges and seep 4 (vertical exaggeration 7×). Black arrows delineate the top of the acoustic wipeout zone. (B) Chimney meta-attribute overlay showing only the highest-probability (>80%) chimney detections. Note the bottom-simulating change in acoustic character and disrupted reflectors, or pipes, that extend upsection from the gas-wipeout zone to the seep site.**

along this section is more rugged and morphologically diverse and displays a greater degree of tectonic influence than the northern section (Brothers et al., 2019; Greene et al., 2019). Although the seafloor trace of the QCF remains confined to a narrow zone of deformation, a series of elongate ridgelines to the west of the QCF are bounded by steep escarpments and are either incised by or have deflected the processes of submarine canyon erosion (Fig. 2B). The elongate ridgelines are of predominantly tectonic origin (e.g., Tréhu et al., 2015), and all seeps identified along the central section are located on ridgelines. Seeps 7 and 8 are along a ridge crest that defines the edge of the westward-facing escarpment, but the ridge appears to be buried by sediment accumulation along its eastern flank (Figs. 4–6). MCS profiles crossing both seep sites reveal complex patterns of acoustic wipeout, and noticeable shoaling of the wipeout zone occurs beneath both seep sites. The chimney analysis shows evidence for disrupted reflectors, or pipes, extending vertically from the wipeout regions to the seep sites (Figs. 4 and 5). Although these high-resolution MCS profiles do not show definitive evidence for bottom-simulating changes in character, cross-cutting reflections are observed along the flanks of the anticlinal ridge and may be related to the base of the GHSZ (Figs. 4–6; Fig. S17 [footnote 1]). Seeps 9, 10, and 11 are located along a fault-controlled anticlinal ridgeline that extends across the international border (see Tréhu et al., 2015, their figure 6). The ridgeline is 10–20 km west of the QCF and does not appear to be directly related to the QCF in its present-day configuration. Sites 10 and 11 appear to be clustered sets of seeps along linear alignments ~500 m long (Fig. 7). The sparker MCS data did not provide adequate penetration and imagery of the internal structure of this steeply flanked ridgeline. Seep 12 is located along an anticlinal structure similar to that of seeps 9–11, and a nearby airgun MCS profile (EW9412 line 1263; Fig. 7) contains a bottom-simulating reflector beneath the projected seep site that was previously inferred to represent a zone of free gas trapped beneath the base of the GHSZ (Riedel et al., 2020).

Based on this study, a total of six seeps were identified along the southern section of the QCF, with all seeps except 13 and 18 located along structurally controlled morphology within the Queen Charlotte terrace (Fig. 2C). Along the southern section of the QCF, the slope morphology is complex


Downloaded from http://pubs.geoscienceworld.org/gsa/geosphere/article-pdf/16/6/1336/5182833/1336.pdf
by MBL WHOI Library user

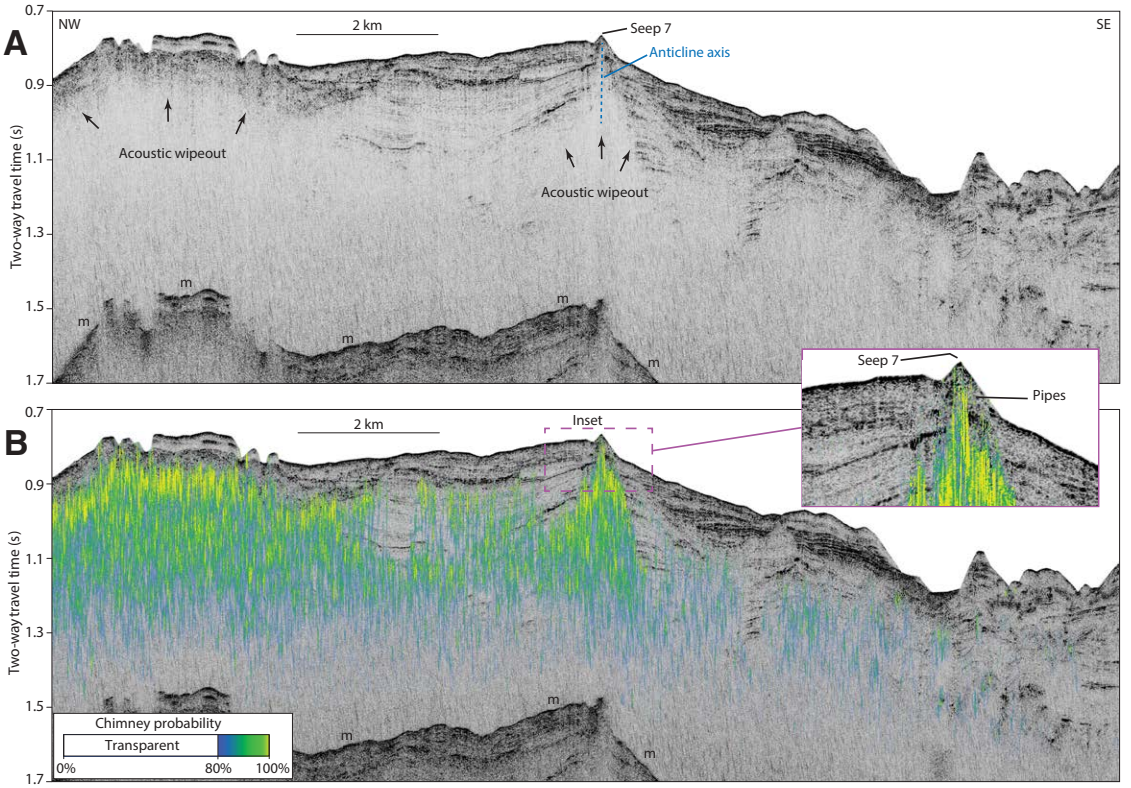


**Figure 4. (A) Multichannel seismic reflection profile (see Fig. 2B for location) crossing seep 7 and the axis of a buried anticline (vertical exaggeration 7×). (B) Chimney meta-attribute overlay showing only the highest-probability (>80%) chimney detections. Note the acoustic-wipeout zone (black arrows) that extends upsection toward the seep site; the enlarged inset shows a series of vertical pipes illuminated by high chimney probabilities. The seafloor multiple (m) is a data artifact.**

and rugged. This most likely reflects an increase in the degree of oblique convergence accommodated by the QCF in the south. Seep 13 lies ~4 km southwest of the QCF and is associated with a slide mass located on a bathymetric high formed on the west side of the fault, possibly emanating adjacent to a slide block within the slide zone (Greene et al., 2019). Seep 14 occurs along the trace of the QCF, seep 18 is located along the shelf edge of southernmost Haida Gwaii, and seeps 16–17 occur at the top of two broad, rounded bathymetric promontories (Fig. 2C) that were constructed through the transport of both sediment (mud) and fragments of mafic rock to the surface. Previous observations from Barrie et al. (2020) documented mud rivulets on the upper flanks of the cone-like structures and the presence of basaltic fragments with manganese crusts as well as authigenic carbonate from the summits of these edifices. These observations are consistent with evidence used by Paull et al. (2015) to identify mud volcanoes in the Beaufort Sea (Arctic Alaska and Canada). Seep 15 occurs near the top of the western flank of a similar-sized round, but flat-topped, guyot-like mass (e.g., wave-base eroded; Barrie et al., 2013) ~10 km northwest of these cone-like features. The Pacific crust is only ca. 5 Ma at this latitude and gets progressively younger southward to the Explorer Ridge. Seismic reflection data along the southern section of the QCF are limited, but previous studies have documented evidence for transpressional deformation, anticlinal folding, elevated geothermal anomalies, and gas hydrate (Hyndman and Hamilton, 1993; Riedel et al., 2020; Rohr et al., 2000). For example, the occurrence of gas hydrates along the Haida Gwaii margin was recently described in Riedel et al. (2020) using seismic reflection data to identify gas hydrate–related bottom-simulating reflectors.

## X-Ray Diffraction and Petrography

The carbonates sampled from along the QCF represent a suite of authigenic carbonates consisting of fossils, peloids, and intraclasts embedded in a microcrystalline matrix. Aragonite dominates the authigenic carbonates and is the major component in all the samples except for 2017-STN03


Downloaded from http://pubs.geoscienceworld.org/gsa/geosphere/article-pdf/16/6/1336/5182833/1336.pdf
by MBL WHOI Library user

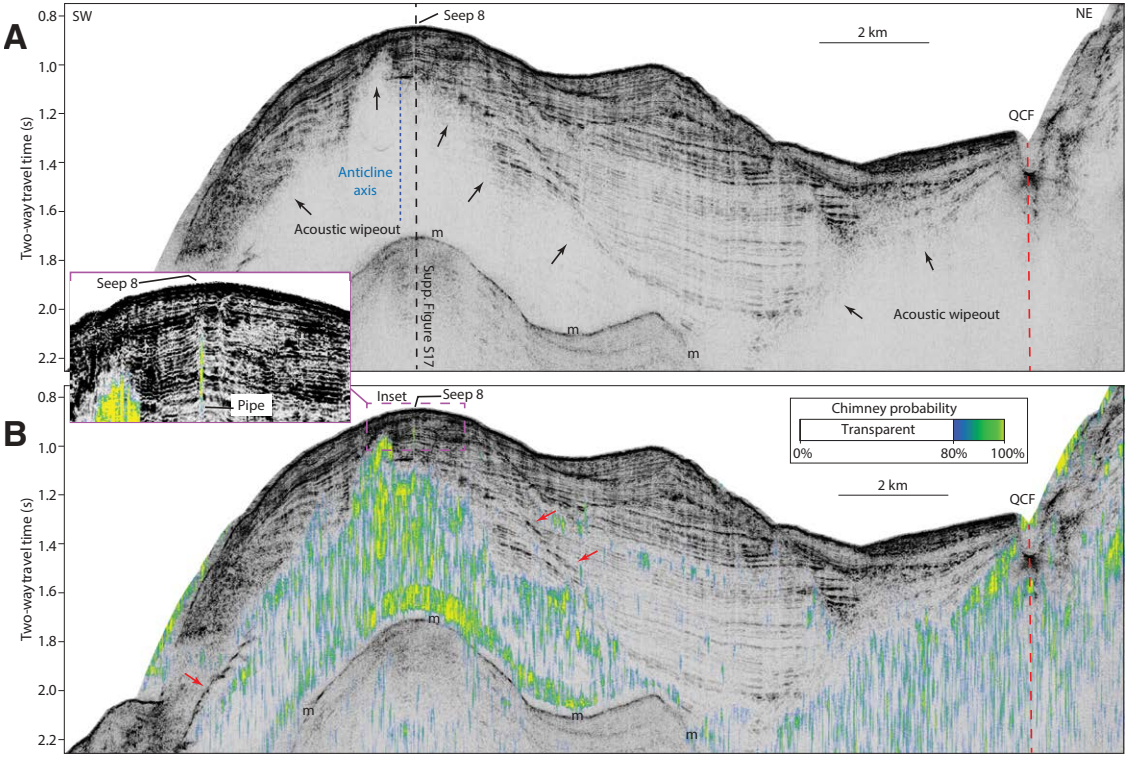


**Figure 5. (A) Multichannel seismic reflection profile (see Fig. 2B for location) crossing seep 8 and the axis of a buried anticline (vertical exaggeration 6×) (see a crossing line in Fig. S17 [text footnote 1]). (B) Chimney meta-attribute overlay showing only the highest-probability (>80%) chimney detections. Note the acoustic-wipeout zone (black arrows) that extends upsection toward the seep site; the enlarged inset shows a series of vertical pipes illuminated by high chimney probabilities. Red arrows denote a series of reverse-polarity reflections that appear to be bottom simulating. The seafloor multiple (m) is a data artifact. QCF—Queen Charlotte fault.**

(seep 11) where dolomite is the major carbonate phase (Table 2). Dolomite is present in two other samples (2015-STN35-2 and 2017-STN41-3) as moderate and minor (2017-STN40-3SH) contributions. The contribution from calcium carbonate ($CaCO_3$) ranged between 7% and 97%, suggesting a range of contributions from sedimentary detritus. The carbonates are a combination of highly compacted, low-porosity mudstones and breccias with clastic grains and carbonate pore filling. Moderate contributions were from quartz, low-Mg calcite, and plagioclase, and minor contribution from kaolinite. In addition to quartz, framework grains include K-feldspar and plagioclase, as well as amphibole, mica, and pyroxene (Table 2). Both foraminifera and shell fragments were identified in thin section (samples 2017-STN40 and 2017-STN41; Figs. 6D, 6F). Samples identified as containing fragments of bivalve shell material typically were enriched in $CaCO_3$ (e.g., sample 2017-STN40-2SH), whereas anomalously low $CaCO_3$ characterized quartz-rich subsamples (e.g., sample 2017-STN40-4-1). As described below, several samples contained fractures, veins, and detrital components, with carbonate cement occupying these pore-filled zones. The veins are typically filled with acicular or microcrystalline aragonite, representing two phases of aragonite where the latter signifies diffuse flow of fluids (Peckmann et al., 2009).

The textural, compositional, and morphological features of carbonate precipitation based on thin sections of six individual authigenic carbonate hand specimens include the following: (1) macroporosity with voids and fractures, with cross-cutting veins and acicular pore filling of highly cemented, matrix-supported mudstone with a clotted texture in groundmass (sample 2017-STN15; Figs. 8B, 8C), indicative of a high-energy environment and multiple stages of precipitation; (2) highly compacted, detrital-rich breccia with intact foraminiferal shells (sample 2017-STN40; Fig. 6D) with the lack of veins or cross-cutting representing a less-developed precipitation stage; (3) poorly sorted, fine-grained aragonite breccia with secondary infilling by microcrystalline and acicular pore filling, and inclusion of bivalves and diatoms (sample 2017-STN41; Fig. 6F); (4) lithified, well-sorted dolomite mudstone with scattered clastic grains and highly cemented "rhombs" in a fine-grained crystalline matrix (sample 2017-STN03; Figs. 7B, 7C); (5) poorly sorted and highly compacted, microcrystalline aragonite with


Downloaded from http://pubs.geoscienceworld.org/gsa/geosphere/article-pdf/16/6/1336/5182833/1336.pdf
by MBL WHOI Library user

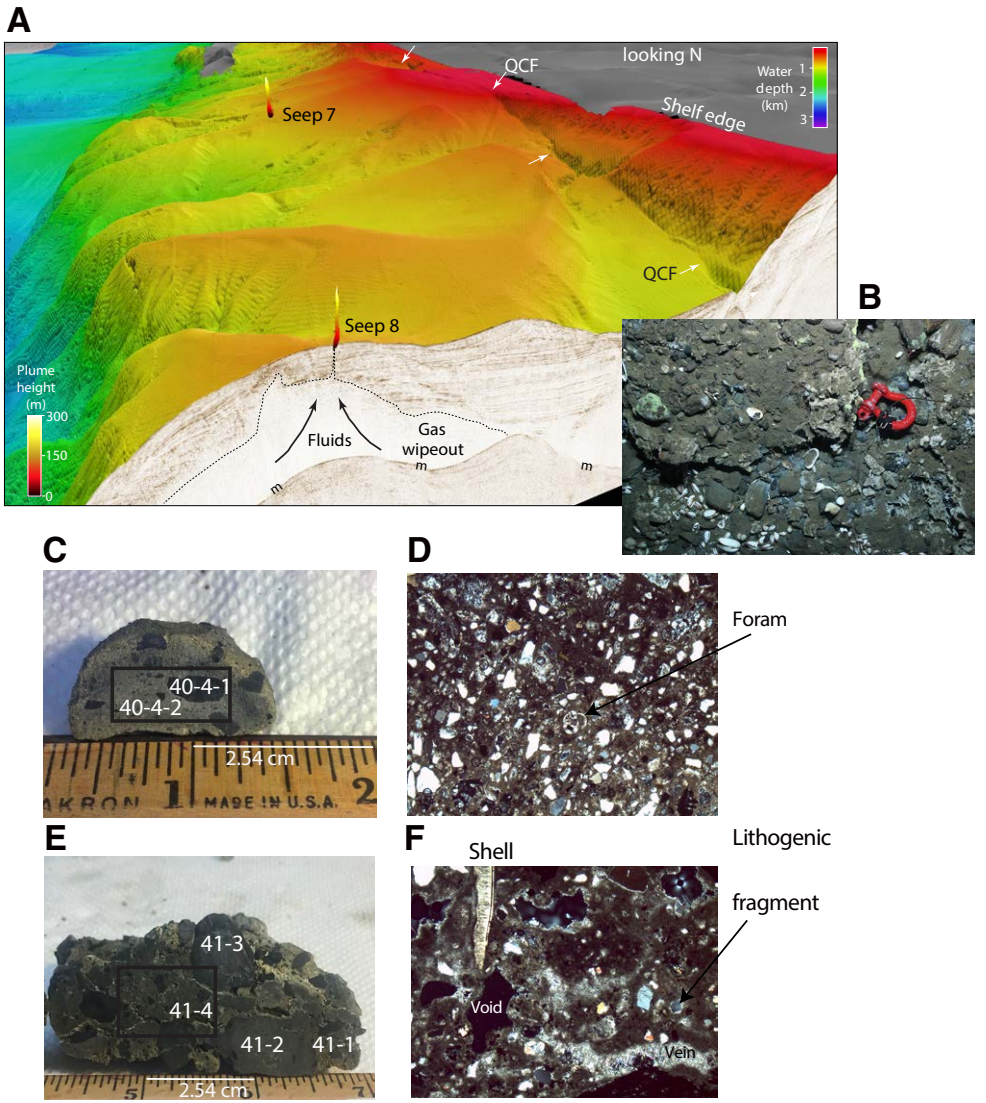


**Figure 6. (A) Three-dimensional perspective view of the seafloor around seeps 7 and 8, including a cutaway along the multichannel seismic reflection profile shown in Figure 5 (vertical exaggeration 4×). White arrows are the surface trace of the Queen Charlotte fault (QCF), and dashed lines define the top of the acoustic-wipeout zone beneath the axis of an anticline, suggesting upsection fluid migration toward the seep site (black arrows). The seafloor multiple (m) is a data artifact. This is a perspective view so it varies, but in the foreground the figure is about 20 km across. (B) In situ photograph of sampling site 2017-STN41 (red shackle is 9 cm wide). (C–F) Photographic and petrographic thin-section images (plane polarized light; 4×) of the authigenic carbonate samples 2017-STN40 (C–D) and 2017-STN41 (E–F). Field of view (length) on petrographic thin-section images is 1000 µM.**

low porosity, and angular quartz detrital components (sample 2011-STN43; Fig. 9D); and (6) breccia with cross-cutting veins, acicular pore filling, and micrite and/or microcrystalline pore-filling cement, suggestive of multiple generations of carbonate precipitation, and clotted microfabric consistent with peloid formation from microbial metabolic processes (Kiel et al., 2013) (sample 2017-STN65; Fig. 9F).

## Stable Isotopes

Authigenic carbonate $\delta^{13}C$ values ranged from –46.82‰ to –2.96‰ (Fig. 10). Samples that were identified as containing shell material were consistently enriched in $^{13}C$ (Table 2). The presence of shell material and seawater-like $^{87}Sr/^{86}Sr$ values, as discussed below, suggests that the authigenic carbonates most likely formed at or near the sediment interface. As such, incorporation of seawater dissolved inorganic carbon during precipitation could help explain the high $\delta^{13}C$ values in these samples relative to methane-derived carbon. However, additional sources of $^{13}C$ enrichment could include AOM, which can generate $^{13}C$ enrichment of the residual $CH_4$ due to preferential microbial oxidation of lighter $CH_4$ (Claypool et al., 1985; Whiticar and Faber, 1986), carbonate reduction methanogenesis from highly enriched $^{13}CO_2$ sources, as well as incorporation of marine carbonate (0‰) and sedimentary organic carbon (–20‰). The carbonate $\delta^{18}O$ values ranged from –6.89‰ to 6.44‰, with samples 2017-STN03 and 2017-STN41-3 accounting for the $^{18}O$-depleted values (Fig. 10). Bottom-water $\delta^{18}O$ values are not available from these sites. However, the $\delta^{18}O$ range yields unrealistically cold bottom-water temperatures (<0 °C) based on the aragonite-temperature equation of Grossman and Ku (1986). In situ temperatures from the CTD rosette casts range between 3.03 and 4.10 °C, suggesting an aragonite $\delta^{18}O$ value between 2.6‰ and 2.85‰. Only 12% of the aragonite $\delta^{18}O$ values fall within this range, with the majority of aragonite $\delta^{18}O$ values suggesting input from an $^{18}O$-enriched fluid source. In contrast, the $^{18}O$-depleted samples 2017-STN03 (seep 11) and 2017-STN41-3 (seep 8) may reflect warmer temperatures and/or the influence of $^{18}O$-depleted fluids.


Downloaded from http://pubs.geoscienceworld.org/gsa/geosphere/article-pdf/16/6/1336/5182833/1336.pdf
by MBL WHOI Library user

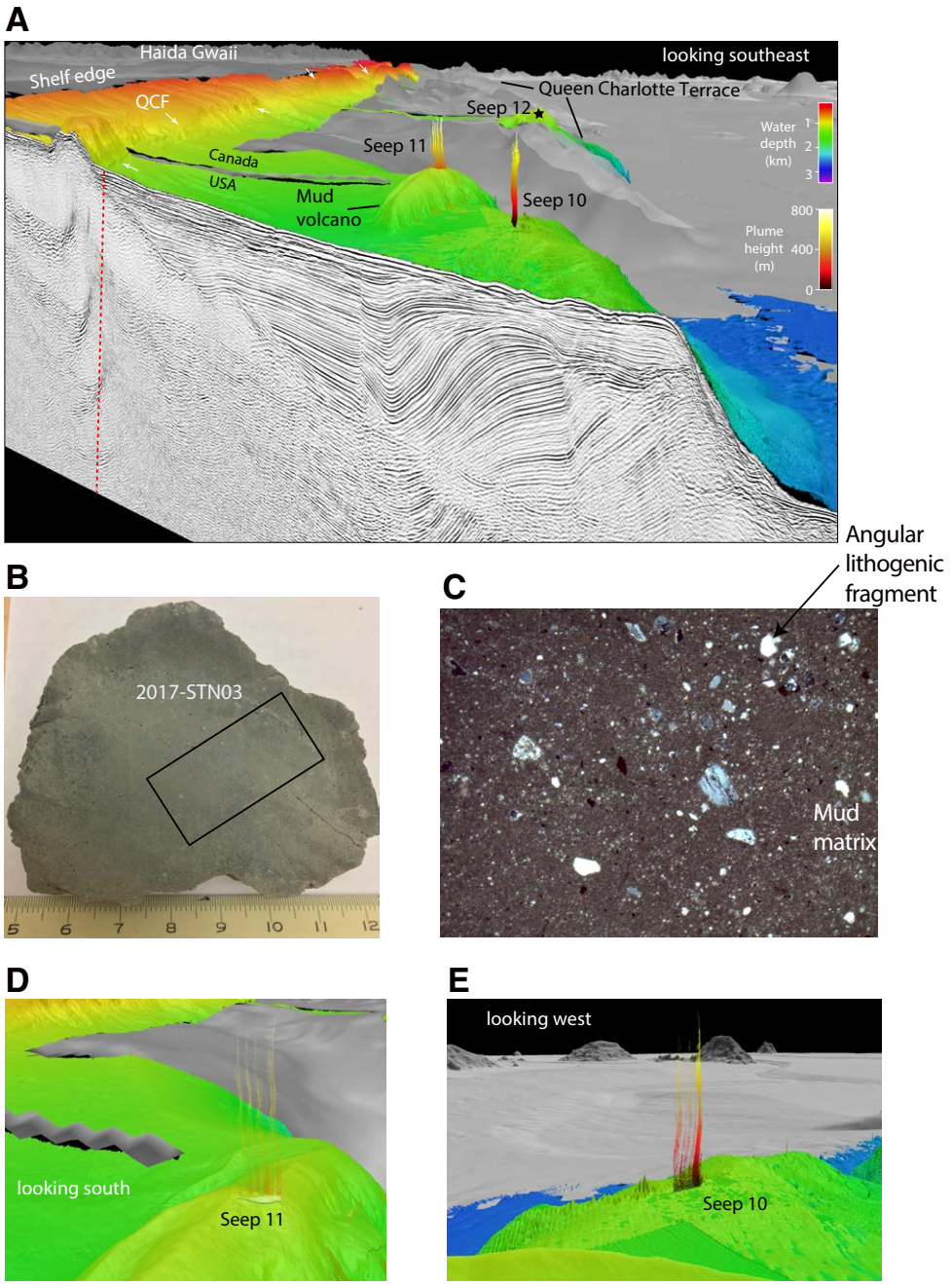


**Figure 7. (A) Three-dimensional (3-D) perspective view of the seafloor around seeps 10, 11, and 12 along the crest of an anticlinal ridgeline near the USA-Canada international border. The cutaway is showing subseafloor acoustic reflections from a seismic reflection profile. The dashed red line is the Queen Charlotte fault (QCF). This is perspective view, and scale in the foreground is ~5 km across. (B–C) Photographic (B) and petrographic (C) thin-section images (plane polarized light; 4×) of the authigenic carbonate sample 2017-STN03. Field of view (length) on the petrographic thin-section image is 1000 µM. (D–E) Enlarged 3-D perspective views of seeps 10 and 11, which are characterized by clusters of multiple seeps across a ~500 m span. This is perspective view, and scale in the foreground is ~5 km across.**

The range in $^{87}Sr/^{86}Sr$ of the carbonates was from 0.708922 to 0.709158 (Table 2). Compared to modern seawater, with $^{87}Sr/^{86}Sr$ of 0.709175 (Paytan et al., 1993), two of the authigenic carbonate samples, 2017-STN03 (seep 11) and 2011-STN43-1 (seep 16), yielded less-radiogenic values. These $^{87}Sr/^{86}Sr$ values were lower than modern seawater by as much as 0.000253, whereas the majority of samples yielded seawater-like $^{87}Sr/^{86}Sr$ values with an offset of <0.00008 compared to modern seawater.

## U-Th Age

Discrete subsamples of cavity-filling authigenic carbonate weighing between 0.81 and 75.14 mg were hand-drilled from five of the QCF specimens. These samples were chosen for U-Th dating given evidence of relatively pure late-stage cavity-filling carbonate cements. The specimens contain 1.99–5.62 ppm U and 0.09–0.90 ppm Th. ($^{230}Th/^{232}Th$) activity ratios were between 2.6 and 6.2, at the lower end of the range reported for other methane-related authigenic carbonates in the literature (Bayon et al., 2009; Crémière et al., 2013; Feng et al., 2015; Teichert et al., 2003). Therefore, a detrital correction is required, as discussed above. Following this correction, several of the specimens yielded initial $(^{234}U/^{238}U)_i$ values offset from the modern seawater $^{234}U/^{238}U$ of 1.1466 (Robinson et al., 2004), an indication that the carbonates have exchanged U and/or Th with their environment


Downloaded from http://pubs.geoscienceworld.org/gsa/geosphere/article-pdf/16/6/1336/5182833/1336.pdf
by MBL WHOI Library user

TABLE 2. CARBONATE GEOCHEMISTRY

| Sample ID* | Total carbon (%) | Total organic carbon (%) | Total inorganic carbon (%) | Calcium carbonate (%) | $\delta^{13}C$ (‰) | $\delta^{18}O$ (‰) | $^{87}Sr/^{86}Sr$ | 2σ | U-Th age# (ka) (error) | Major (>25%) | Moderate (5%–25%) | Minor (<5%) |
|---|---|---|---|---|---|---|---|---|---|---|---|---|
| 2017-STN15-1 | 4.42 | 0.32 | 4.10 | 34.16 | –32.34 | 2.76 | 0.709107 | 0.000017 | 3.50–3.76 (± 1.02–1.49) | Aragonite, quartz | Plagioclase | Kaolinite, amphibole, LMC |
| 2017-STN15-2 | 10.08 | 1.61 | 8.47 | 70.55 | –33.07 | 3.19 | | | | Aragonite, quartz | Plagioclase | LMC |
| 2017-STN15-3 | 4.68 | 0.28 | 4.40 | 36.63 | –30.64 | 2.22 | | | | Aragonite, quartz | Plagioclase, K-spar†† | Kaolinite |
| 2017-STN15-4 | 9.08 | 0.56 | 8.52 | 71.02 | –30.86 | 3.06 | | | | Aragonite, quartz, plagioclase | LMC, barite | |
| 2017-STN04-2-1 | N.A.§ | N.A. | N.A. | N.A. | –11.52 | 4.22 | | | | Aragonite | LMC | Plagioclase |
| 2017-STN04-2-2 | N.A. | N.A. | N.A. | N.A. | –2.96 | 4.54 | | | | N.A. | N.A. | N.A. |
| 2017-STN04-2-3 | N.A. | N.A. | N.A. | N.A. | –21.36 | 4.34 | | | | Aragonite | Quartz, plagioclase | Kaolinite, LMC |
| 2017-STN03 | 8.43 | 0.08 | 8.36 | 69.63 | –13.94 | –6.89 | 0.708922 | 0.000022 | | Dolomite | Quartz, plagioclase (albite) | Pyroxene, chlorite, illite, amphibole |
| 2015-STN34-1 | 5.16 | 0.04 | 5.13 | 42.73 | –12.41 | 3.54 | 0.709151 | 0.000019 | | Aragonite, quartz, | Plagioclase | Kaolinite, LMC |
| 2015-STN35-1 | 6.73 | 0.01 | 6.72 | 55.97 | –36.44 | 6.44 | 0.709158 | 0.000022 | | Ankerite | Quartz, plagioclase, K-spar | Kaolinite |
| 2015-STN35-2 | 7.89 | 0.22 | 7.67 | 63.92 | –32.10 | 5.64 | | | | LMC** | Plagioclase, dolomite, HMC§§ | |
| 2017-STN40-1 | 5.43 | 0.11 | 5.31 | 44.27 | –36.35 | 3.16 | 0.709104 | 0.000024 | | Aragonite, quartz | Plagioclase | Kaolinite, amphibole, LMC, witherite |
| 2017-STN40-2 | 3.99 | 0.17 | 3.81 | 31.77 | –33.24 | 2.78 | | | | Aragonite, quartz | N.A. | LMC, kaolinite |
| 2017-STN40-2SH† | 11.73 | 0.08 | 11.65 | 97.06 | –9.80 | 4.41 | | | | Aragonite | LMC, K-spar | |
| 2017-STN40-3 | 4.58 | 0.63 | 3.96 | 32.98 | –33.50 | 2.98 | | | | Aragonite, quartz | Plagioclase, K-spar | Kaolinite |
| 2017-STN40-3SH | 11.77 | 1.71 | 10.06 | 83.85 | –12.62 | 4.35 | | | | Aragonite | LMC | Dolomite |
| 2017-STN40-4-1 | 1.80 | 0.97 | 0.83 | 6.92 | –32.28 | 2.71 | | | | Quartz | Mica, plagioclase | Kaolinite |
| 2017-STN40-4-2 | 4.53 | 1.13 | 3.40 | 28.31 | –33.77 | 3.36 | | | | Aragonite, quartz, plagioclase | | Kaolinite, amphibole, mica/illite |
| 2017-STN41-1 | 6.69 | 0.98 | 5.72 | 47.63 | –29.97 | 3.69 | 0.709139 | 0.000021 | | Aragonite, quartz | Plagioclase | Kaolinite, K-spar, LMC |
| 2017-STN41-2 | 6.31 | 0.38 | 5.93 | 49.41 | –33.18 | 3.77 | | | | Aragonite, quartz | Plagioclase | Kaolinite, K-spar, LMC |
| 2017-STN41-3 | 4.41 | 3.20 | 1.21 | 10.10 | –14.39 | –6.65 | | | | Quartz | Dolomite | Plagioclase, amphibole |
| 2017-STN41-4 | 7.18 | 0.57 | 6.61 | 55.06 | –31.25 | 3.48 | | | | Aragonite, quartz | Plagioclase | LMC, kaolinite, K-spar |
| 2011-STN43-1 | 3.53 | 0.18 | 3.35 | 27.93 | –45.77 | 3.48 | 0.708939 | 0.000024 | | Quartz, aragonite, plagioclase | | Kaolinite, amphibole |
| 2011-STN43-2 | 3.94 | 0.06 | 3.88 | 32.29 | –46.82 | 3.61 | | | | Quartz, aragonite, plagioclase | | Kaolinite, amphibole |
| 2017-STN65-1 | 8.51 | 0.61 | 7.90 | 65.83 | –31.85 | 4.35 | | | 17.55–20.00 (± 2.59–2.91) | Aragonite, quartz | Plagioclase, LMC | Amphibole |
| 2017-STN65-2 | 8.24 | 0.16 | 8.08 | 67.36 | –33.85 | 4.12 | | | | Aragonite, quartz | Plagioclase | LMC, K-spar |
| 2017-STN65-3 | 8.41 | 0.04 | 8.36 | 69.70 | –33.98 | 4.26 | | | | Aragonite, quartz | Plagioclase | LMC, amphibole, halite |

*Note:* The relative percentage of carbonate minerals within each sample is expressed as major, moderate, or minor.
*Individual authigenic carbonate samples were subsampled, and sample identification includes subset number (e.g., "-2").
†SH—shell.
§N.A.—not applicable. Because of small sample size, carbon analysis was not performed on 2017-STN04-2.
#See Table S1 (text footnote 1) for detailed U-Th analysis.
**LMC—low-magnesium calcite.
††K-spar—potassium feldspar.
§§HMC—high-magnesium calcite.


Downloaded from http://pubs.geoscienceworld.org/gsa/geosphere/article-pdf/16/6/1336/5182833/1336.pdf
by MBL WHOI Library user

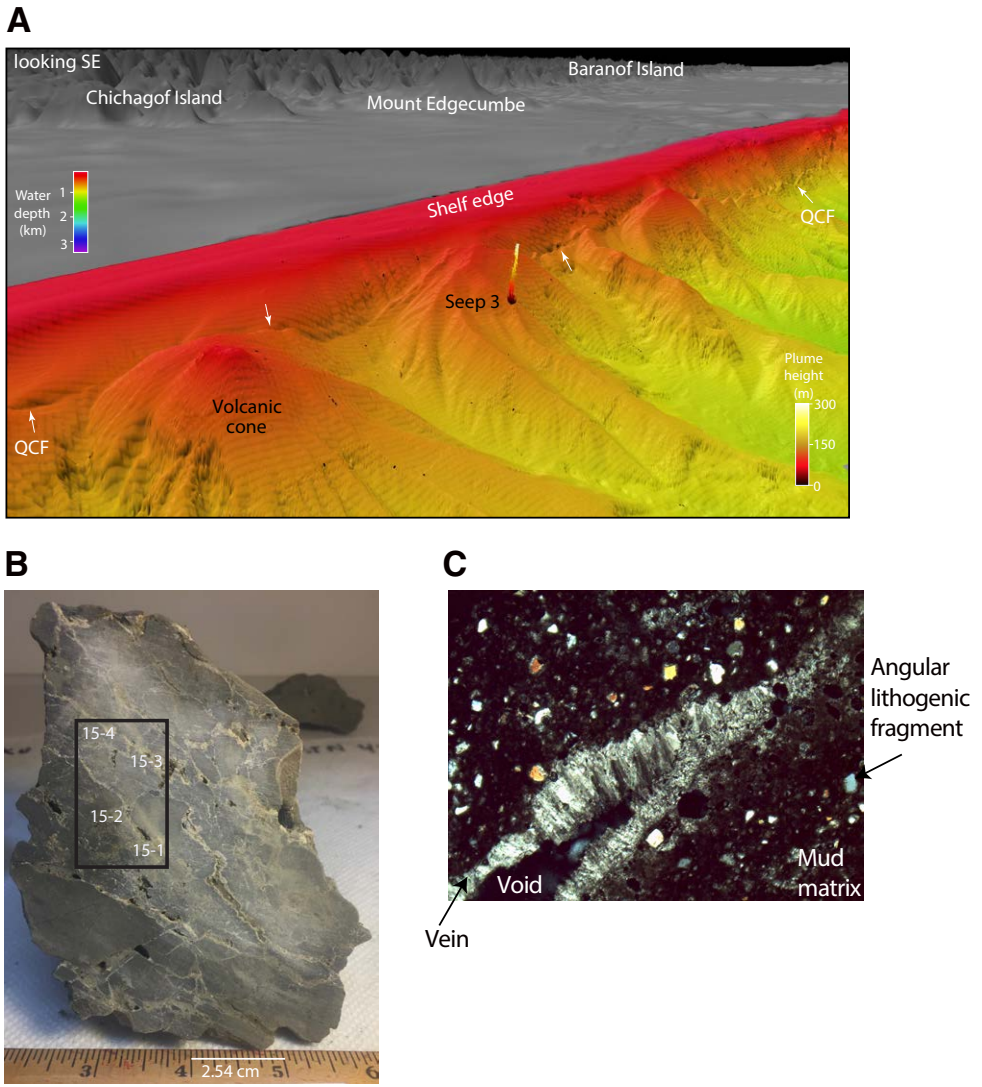


**Figure 8. (A) Three-dimensional perspective view of the seafloor around seep 3, located ~2 km west of the Queen Charlotte fault (QCF; white arrows) (vertical exaggeration 4×). Seep 3 is located between two known volcanic features: Mount Edgecumbe, and a recently discovered volcanic cone to the west of the QCF (Barrie et al., 2020). (B–C) Photographic (B) and petrographic (C) thin-section images (plane polarized light; 4×) of an authigenic carbonate sample from seep 3 (2017-STN15). Field of view (length) on the petrographic thin-section image is 1000 µM.**

since precipitation, which results in inaccurate calculated ages. Therefore, only two specimens, for which the $(^{234}U/^{238}U)_i$ from late-stage carbonate precipitates was within uncertainty of the modern seawater value, were deemed to have reliable dates: samples 2017-STN65 (ca. 19 ka) and 2017-STN15 (ca. 3.6 ka) (Table S2 [footnote 1]).

### Gas Geochemistry

The composition of the void gas from this site was dominated by methane (99%), with ethane and propane contributing at 690 ppm and 6 ppm (Table 3). The $\delta^{13}C$ value of the void gas was –47‰ and yielded a $C_1 / (C_2 + C_3)$ ratio of 1230. Sediment gas extracted from the headspace of a canned core-cutter sample was also dominated by methane and had a similar methane isotopic composition (–44‰) to the void gas and a lower hydrocarbon $C_1 / (C_2 + C_3)$ ratio of 240, a result consistent with the preferential loss of methane due to sediment degassing during core recovery.

## DISCUSSION

### Geologic Framework of Seep Genesis

The seismic data and associated attribute calculations along the QCF suggests that both active and dormant venting along the margin are stratigraphically and structurally controlled by anticlinal features located away from the QCF instead of narrowly focused along the QCF. The fact that seeps along the QCF were not observed in abundance may suggest that the QCF strike-slip fault is generally not a zone of gas accumulation; instead, methane traps develop away from the fault in structural and sedimentary anticlines. The occurrence of seeps away from the QCF is compatible with conceptual models of focused fluid flow and gas migration along the crest of an anticline (Paull et al., 2008), such as observed offshore northern Panama (Reed et al., 1990), where folding, thrust faulting, and sedimentation along a deformation front may facilitate fluid flow and seafloor venting


Downloaded from http://pubs.geoscienceworld.org/gsa/geosphere/article-pdf/16/6/1336/5182833/1336.pdf
by MBL WHOI Library user

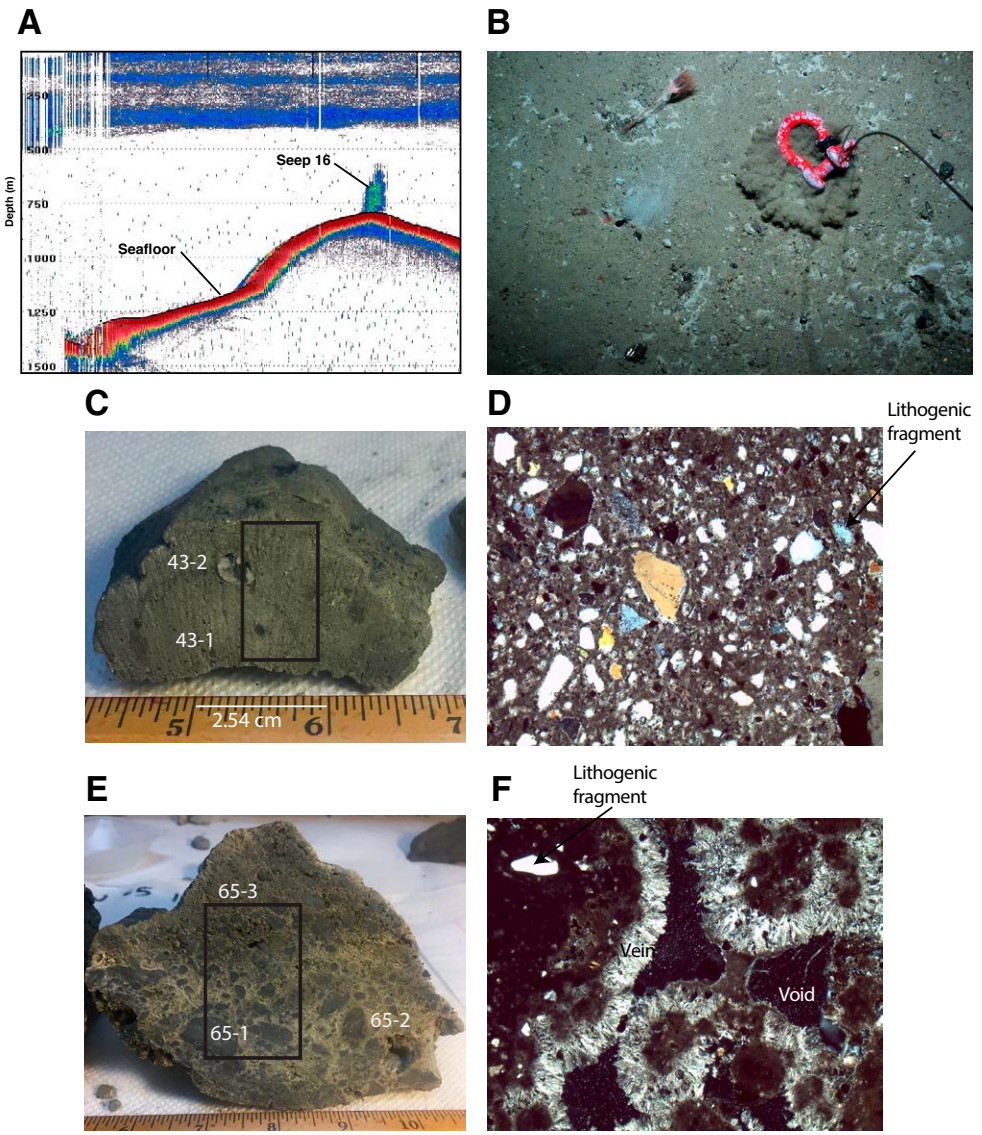


**Figure 9. (A) Water-column plume from 18kHz profile of seep 16. Colors reflect intensity of acoustic return, red (warmer) colors are high intensity and blues are lower. There is a scale bar on the y-axis indicating water depth. Horizontal depth is not provided on the EK60 profiles since this is dependent on ship speed and ping rate. (B) In situ photograph of sample site (2017-STN64). (C–F) Photographic and petrographic thin-section images (plane polarized light; 4×) of the authigenic carbonate sample 2011-STN43 (C–D) and 2017-STN65 (E–F). Field of view (length) on petrographic thin-section images is 1000 µM.**

(Fig. 11). The absence of abundant fluid flow along the QCF could also be partially due to the lack of transpressional and transtensional deformation along the majority of the fault's length (Brothers et al., 2020). This more pure translational motion along the fault differs from other more obliquely striking offshore strike-slip faults and/or plate boundaries (e.g., Dupré et al., 2015), limiting the vertical deformation of surrounding strata (extensional and compressional). This lack of deformation prevents the development of structures that promote updip fluid flow and trapping. However, the active seeps and subsurface fluid-flow indicators presented in this study are extracted from data sets with limited spatial coverage and detection abilities and thus likely represent just a fraction of the total seep distribution along the QCF margin. For example, two sites located directly on the active trace of the QCF (seeps 5 and 14) were not sampled because of weather constraints, but both likely represent fluid migration along the fault zone.

Although the continental slope along the northern section of the QCF appears to be dominated by marine sedimentary processes (incised networks of submarine canyons and emplacement of fan aprons) rather than by tectonic deformation (Brothers et al., 2019), the seeps are in several different geomorphic environments. This includes localized areas of transpression along a transform fault and sedimentary loading due to rapid sedimentation from Quaternary glacial processes. In some cases, these processes manifest as seeps at topographic crests where gas is trapped, possibly beneath the low-permeability base of the GHSZ (e.g., Bünz et al., 2012; Petersen et al., 2010). Therefore, seeps sampled in this study appear to preferentially occur along the crests of ridgelines formed by (1) incision and/or aggradation surrounding submarine canyons and (2) folding and uplift along contractional structures.

We propose that sedimentary aggradation along canyon interfluves coupled with incision in the thalwegs generates lenticular beds that resemble structural anticlines and promote updip fluid migration and trapping. We propose updip migration of fluids from underlying hydrocarbon reservoirs. This interpretation is further warranted given that


Downloaded from http://pubs.geoscienceworld.org/gsa/geosphere/article-pdf/16/6/1336/5182833/1336.pdf
by MBL WHOI Library user

the authigenic carbonate precipitates and areas of active venting are located on the spines or crests of ridges (Figs. 1, 2, 7A, 8A). In cross-section, these ridges are antiformal structures that are flanked by growth faults and growth strata depicting recent deformation (Walton et al., 2018). The development of anticlinal ridges is a key feature along the QCF that facilitates focused fluid flow where the plate boundary is obliquely convergent. This scenario is similar to that observed in Southern California where fluid migration is controlled by fault-segment boundaries where folding and convergent deformation occur along strike-slip faults (Kluesner and Brothers, 2016; Maloney et al., 2015) and along other active margins characterized by folding and shortening within the accretionary wedge (Carson et al., 1991, 1994; Johnson et al., 2003; Reed et al., 1990). Upward fluid migration is further enhanced where pore-fluid pressure gradients are increased as a result of sediment loading and compaction, which facilitates transportation to the seafloor.

The high-resolution MCS data in the study region show bottom-simulating changes in character and acoustic wipeout (Figs. 3–5), which are commonly seismic indicators for the hydrate–free gas interface (Chand and Minshull, 2003) and sometimes referred to as gas wipeout. We also observe gas wipeout along the upper limbs and axes of lenticular bedding planes, suggesting updip fluid migration within a chimney structure (Løseth et al., 2009). Similar observations are found along the structurally controlled ridgelines of the central and southern sections of the margin. The neural-network chimney attribute calculations on seismic profiles help delineate broad chimney features and more focused and/or narrow zones of fluid migration referred to as "pipes" (e.g., Fig. 3B inset). The attribute calculation is focused on highlighting vertical zones of discontinuity and regions with significant vertical change in the frequency content of the data (Kluesner and Brothers, 2016). Such zones highlighted by the attribute calculation in the data commonly simulate the seafloor bottom reflection, likely delineating the isothermally controlled transition from frozen hydrate to free methane gas. Due to the high-frequency content of the sparker data, the presence of free gas can result in washout of higher frequencies due to scattering attenuation of the P waves. In addition, narrow vertical zones of discontinuity (pipes) highlighted by the chimney attribute also extend vertically toward the seafloor near the apex of ridges and anticlinal folds (Figs. 3, 4, 5). The pipe

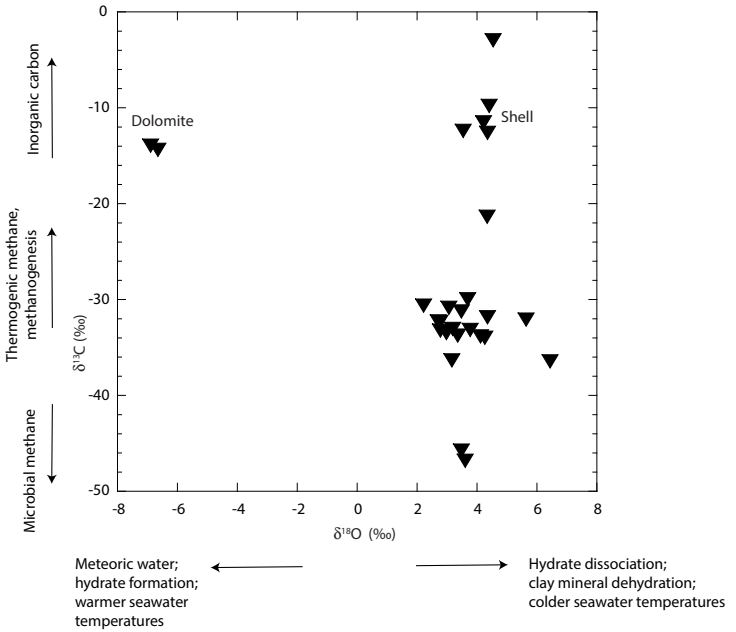


**Figure 10. Relationship between authigenic carbonate stable oxygen ($\delta^{18}O$) and carbon ($\delta^{13}C$) composition (reported in per mil, ‰). End-member sources and/or processes are shown for both $\delta^{18}O$ and $\delta^{13}C$ values. Outliers for the dolomite and bivalve shell sample are labeled.**

TABLE 3. VOID GAS MEASUREMENTS

| Sample ID* | Methane ($C_1$) | Ethane ($C_2$) | Propane ($C_3$) | Isobutane ($iC_4$) | Normal butane ($nC_4$) | Isopentane ($iC_5$) | Normal pentane ($nC_5$) | $\frac{C_1}{(C_2 + C_3)}$ | Methane $\delta^{13}C^{\#}$ (‰) | Methane $\delta^{13}C$ (‰) | Methane $\delta^{13}C$ (‰) |
|---|---|---|---|---|---|---|---|---|---|---|---|
| 2017-STN03 headspace (ppm) | 21498.0 | 89.9 | 0.9 | 0.1 | 0.1 | 0.0 | 0.0 | 240 | –44.54 | –43.90 | –46.00 |
| 2017-STN03 void gas (ppm) | 828490.0 | 677.0 | 5.9 | 0.4 | 0.1 | 0.4 | 0.3 | 1230 | –47.62 | N.A. | N.A. |
| 2017-STN03 void gas (ppm)† | 843440.0 | 690.0 | 5.7 | 0.4 | 0.1 | 0.4 | 0.0 | 1228 | –47.62 | N.A. | N.A. |

*Gas measurements from headspace and void gases at 2017-STN03 (seep 11).
†Duplicate sample.
#Carbon isotope gas-chromatograph replicates; N.A. indicates not analyzed.


Downloaded from http://pubs.geoscienceworld.org/gsa/geosphere/article-pdf/16/6/1336/5182833/1336.pdf
by MBL WHOI Library user

features commonly root into the broad chimney zones, likely acting as focused pathways for fluid and/or gas escape (e.g., Fig. 5B inset). Such pipe-like features have been observed in seismic data from other regions and have been interpreted as fluid-migration pathways and episodic gas blowout structures (Løseth et al., 2009).

The observation of chimneys and disappearance or shoaling of the inferred free gas–hydrate interface below seep sites may be due to heat transport by ascending fluids that contribute to zones of hydrate destabilization. The warmer ascending fluids can trigger destabilization by heating the adjacent sediments, promoting the release of hydrate-derived methane (Davis et al., 1995; Mann and Kukowski, 1999; Wood et al., 2002). This scenario provides a potential source of $^{18}O$-enriched fluids through hydrate dissociation, which releases hydrate water and contributes to enrichment by as much as 3.5‰ (Maekawa, 2004). For example, along the Cascadia margin in the northeastern Pacific (Johnson et al., 2015, and references therein), active areas of methane emission occur at the upper limit of the GHSZ near a water depth of 500 m, suggesting that gas hydrate dissociation is a major driving force of methane release along this margin (Johnson et al., 2015). Despite the observation that the upper limit of the GHSZ is near a water depth of 500 m and hydrate should be stable at our sampling sites, it is possible that heating from deeply sourced fluids is exerting a thermal control on hydrate stability and shifting the hydrate phase boundary (Chand and Minshull, 2003). It should also be noted that a direct comparison to the Cascadia margin is confounded by a lack of thermal data along the QCF, which varies in age and therefore thermal structure, which also exerts a primary control on the position of the GHSZ. The QCF carbonate $\delta^{18}O$ values are $^{18}O$ enriched by between 0.13‰ and 3.59‰ relative to predicted values based on the aragonite-temperature equation of Grossman and Ku (1986) using CTD temperatures. This offset suggests isotopic disequilibrium and the influence of an $^{18}O$-enriched fluid source. For example, given the age of the authigenic carbonate sample 2017-STN65 (seep 17; 17.55–20.00 ka), a shift in the GHSZ during the Last Glacial Maximum (LGM) can explain the $^{18}O$-enriched carbonate values. Present-day conditions indicate that seep 17 is well within the GHSZ (800 m water depth and 3.9 °C), requiring either a warming of ~6 °C or a sea-level drop of ~400 m, or possibly a combination. Given that an isostatic forebulge under Haida Gwaii resulted in an early post-glacial relative sea level of ~–150 m below present (Clague, 1983; Josenhans et al., 1997; Shugar et al., 2014), a warming of only 4 °C would have been required to shift the GHSZ. There is evidence of surface warming in the area, with *Globigerina bulloides* recording a range of temperatures from 7.3 to 8.8°C from 21 to 14.7 ka (Taylor et al., 2014). Therefore, it is possible that warming acted in combination with an isostatic crustal forebulge during the LGM to drive hydrate destabilization along the QCF near Haida Gwaii. However, additional pore-fluid chemistry is needed to tease apart the different processes impacting the fluid chemistry, including hydrate dissociation (Davidson et al., 1983) as well as the potential role of clay-mineral dehydration during the smectite-illite transformation that releases interlayer water (e.g., Hensen et al. (2004).

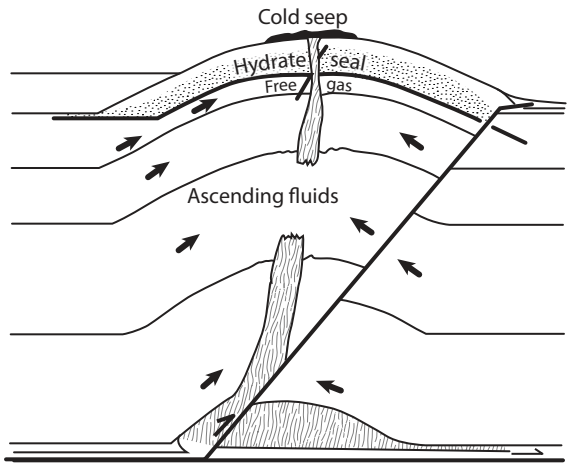


**Figure 11. Schematic diagram of focused flow and updip migration of deep-rooted methane (arrows) into an anticlinal ridge formed from folding, thrust faulting, and sedimentation along a deformation fold. Ascending fluids warm the surrounding strata and trigger hydrate dissociation and release of free gas (modified from Reed et al., 1990). The various lines represent stratigraphic layers.**

## Authigenic Carbonate Formation and Source Fluids

Compaction and degradation of organic-rich sediment, continuously forming hydrocarbon reservoirs (Tinivella and Giustiniani, 2012), and dissolution of clathrates or frozen gas-hydrate systems suggest that fluids could originate from multiple sources as well as evolution pathways along the QCF. The range in $\delta^{13}C$ values from the QCF authigenic carbonates captures mixing between carbon sources (Campbell, 2006). There are three clusters of $\delta^{13}C$ values: $\delta^{13}C > -20‰$, $-30‰ > \delta^{13}C > -40‰$, and $\delta^{13}C < -40‰$ (Fig. 10). Broadly, there are three potential carbon pools with distinct $\delta^{13}C$ values: a heavy marine inorganic carbon pool, enriched thermogenic methane, and depleted microbial methane (Whiticar, 1999). Depleted microbial methane (<–50‰) results from degradation of microbial organic matter within the methanogenic zone (Tissot and Welte, 1984), whereas thermogenic methane results from thermal decarboxylation during burial of organic matter, producing relatively enriched methane (>–40‰) (Bernard et al., 1978). Along the Cascadia margin to the south, both microbial methane and thermogenic hydrocarbon sources have been identified (Sample and Reid, 1998; Teichert et al., 2005), helping to explain the large spatial heterogeneity and complex hydrology of the margin (e.g., Torres et al., 2009). While limited in scope, the single void-gas $\delta^{13}C$ measurement from


Downloaded from http://pubs.geoscienceworld.org/gsa/geosphere/article-pdf/16/6/1336/5182833/1336.pdf
by MBL WHOI Library user

sample 2017-STN03 suggests methane of thermogenic origin, whereas the hydrocarbon composition, defined as the $C_1 / (C_2 + C_3)$ ratio, is more consistent with microbially produced methane (Milkov and Etiope, 2018). However, the paired hydrocarbon composition and $\delta^{13}$C-methane value from sample 2017-STN03 are outside the anticipated mixing line between thermogenic and microbial end members (Bernard et al. 1978), indicating that additional processes should be considered, including anaerobic methane oxidation, which can generate $^{13}$C-enriched methane (Claypool et al., 1985), or, for example, carbonate reduction methanogenesis from highly enriched $^{13}CO_2$ sources like those measured at Integrated Ocean Drilling Program Sites U1327 and U1329 along northern Cascadia (Pohlman et al., 2009). Additional gas samples are needed to further determine the role of microbial alteration and to identify distinct carbon sources. However, based on the geophysical data, we propose that along the QCF, a deep-rooted methane signature can occur via the presence of active venting and formation of authigenic carbonates on the spines or crests of ridges (Fig. 11). For example, vertical pipes evident in the chimney meta-attribute calculations overlie regions of gas wipeout beneath the ridgelines and suggest that fluid and/or gas migrates from a deeper reservoir zone along a focused pathway to the seafloor (e.g., Fig. 4).

The majority of authigenic carbonate samples yield seawater-like $^{87}Sr/^{86}Sr$ values, consistent with previously recovered authigenic carbonates from the Cascadia slope (Joseph et al., 2013), where shallow precipitation of aragonite triggered by AOM forms authigenic carbonates in anoxic but seawater-ventilated environments, such as observed at Hydrate Ridge (offshore Oregon, USA; Greinert et al., 2001). This scenario is consistent with aragonite formation in open systems at or close to the sediment-water interface and in situ brecciation of weakly consolidated sediment. The incorporation of shells also indicates in situ cementation of chemosynthetic communities that live at the sediment-water interface. In contrast, the depleted radiogenic Sr-isotope composition from samples 2011-STN43 (seep 16) and 2017-STN03 (seep 11) suggests mixing with fluids other than modern seawater, such as deep-sourced mud breccia flow (e.g., Klasek et al., 2019) and meteoric fluids from groundwater circulating at depth due to changes in hydraulic head linked to ice-sheet dynamics (e.g., Person et al., 2007).

## CONCLUSION

Based on an integrated approach using geology, geophysics, and geochemistry, we demonstrate that anticlinal features located away from the QCF stratigraphically and structurally control active seepage and are indicators of past fluid expulsion. This is in contrast to the assumption that seeps along strike-slip fault systems are primarily focused along faults. Upward fluid migration of methane is facilitated by sediment loading, compaction, and tectonic and sedimentary processes that result in folded strata and anticlinal traps. Fluids are subsequently transported upward through chimneys, eventually oxidized by archaea carrying out AOM and favoring precipitation of authigenic carbonates. Carbonate microstructures in the thin sections including brecciation and pore-filling cement suggest rapid release of fluids and/or gases into weakly compacted sediment at or near the sediment interface. The carbonate chemistry of the authigenic carbonate samples highlights both microbial and thermal degradation of organic matter in continental-margin sediments along the QCF and subsequent fluid seepage. The majority of aragonite carbonates formed in the shallow, anoxic subsurface environment with elevated bicarbonate concentration as a result of AOM and fed by the rise of methane-rich fluids. Future studies focused on localized folding and faulting will further test our assumption that anticlinal structures along the QCF create high-permeability regions where conduits form and facilitate upward migration of fluids. Ideally, future work would include submersible dives to collect discrete gas samples and targeted coring to further investigate fluid sources and the presence of hydrates. In doing so, we can greatly expand our predictive capabilities of the geographic extent and geologic origin of focused fluid flow and methane venting along transform boundaries.

#### ACKNOWLEDGMENTS

The authors thank officers and crew of the CCGS *Vector* and CCGS *John P. Tully*; M. Baker (USGS), R. Garrison (UCSC), J. Fitzpatrick, (USGS), N. Vokhshoori (UCSC), and C. Maupin (Texas A&M University, College Station, Texas, USA) for laboratory and sample assistance; and J. Pohlman (USGS) for helpful comments. Input from two anonymous reviewers substantially improved the manuscript. The USGS Coastal and Marine Hazards and Resource Program funded this study. Any use of trade, product, or firm names is for descriptive purposes only and does not imply endorsement by the U.S. Government. Additional geochemical and geophysical data to support this project can be found in Prouty et al. (2019) and Balster-Gee et al. (2017a, 2017b), respectively.

#### REFERENCES CITED

Balster-Gee, A.F., Andrews, B.D., Brothers, D S., ten Brink, U.S., Kluesner, J.W., and Haeussler, P.J., 2017a, Multibeam and multichannel sparker seismic-reflection data between Cross Sound and Dixon Entrance, offshore southeastern Alaska, collected from 2016-05-17 to 2016-06-12 during field activity 2016-625-FA: U.S. Geological Survey data release, https://doi.org/10.5066/F7NG4PTW.

Balster-Gee, A.F., Brothers, D.S., Miller, N.C., Kluesner, J.W., Ebuna, D.R., and East, A.E., 2017b, Multichannel sparker seismic-reflection data of field activity 2016-656-FA, between Icy Point and Dixon Entrance, Gulf of Alaska from 2016-08-07 to 2016-08-26: U.S. Geological Survey data release, https://doi.org/10.5066/F7KP81BQ.

Barrie, J.V., Conway, K.W., and Harris, P.T., 2013, The Queen Charlotte Fault, British Columbia: Seafloor anatomy of a transform fault and its influence on sediment processes: Geo-Marine Letters, v. 33, p. 311–318, https://doi.org/10.1007/s00367-013-0333-3.

Barrie, J.V., Greene, H.G., Brothers, D., Conway, K.W., Enkin, R.J., Conrad, J.E., Lauer, R.M., McGann, M., Neelands, P.J., and East, A., 2018, The Queen Charlotte–Fairweather Fault Zone—A submarine transform fault, offshore British Columbia and southeastern Alaska: Cruise report of 2017003PGC CCGS *Vector* and 2017004PGC CCGS *John P. Tully*: Geological Survey of Canada Open File 8398, 161 p., https://doi.org/10.4095/308327.

Barrie, J.V., Greene, H.G., and Conway, K.W., 2020, Benthic habitats of a mud volcano associated with the Queen Charlotte transform margin along northern British Columbia, Canada and southern Alaska, USA, *in* Harris, P.T., and Baker, E.K., eds., Seafloor Geomorphology as Benthic Habitat: GeoHab Atlas of Seafloor Geomorphic Features and Benthic Habitats (second edition): Amsterdam, Elsevier, p. 825–834, https://doi.org/10.1016/B978-0-12-814960-7.00050-6.

Bayon, G., Henderson, G.M., and Bohn, M., 2009, U-Th stratigraphy of a cold seep carbonate crust: Chemical Geology, v. 260, p. 47–56, https://doi.org/10.1016/j.chemgeo.2008.11.020.

Bayon, G., Henderson, G.M., Etoubleau, J., Caprais, J.-C., Ruffine, L., Marsset, T., Dennielou, B., Cauquil, E., Voisset, M., and Sultan, N., 2015, U-Th isotope constraints on gas hydrate and pockmark dynamics at the Niger delta margin: Marine Geology, v. 370, p. 87–98, https://doi.org/10.1016/j.margeo.2015.10.012.



Downloaded from http://pubs.geoscienceworld.org/gsa/geosphere/article-pdf/16/6/1336/5182833/1336.pdf
by MBL WHOI Library user

Bernard, B.B., Brooks, J.M., and Sackett, W.M., 1978, Light hydrocarbons in recent Texas continental shelf and slope sediments: Journal of Geophysical Research, v. 83, p. 4053–4061, https://doi.org/10.1029/JC083iC08p04053.

Berndt, C., 2005, Focused fluid flow in passive continental margins: Philosophical Transactions of the Royal Society of London A: Mathematical, Physical and Engineering Sciences, v. 363, p. 2855–2871, https://doi.org/10.1098/rsta.2005.1666.

Brothers, D.S., Ruppel, C., Kluesner, J.W., ten Brink, U.S., Chaytor, J.D., Hill, J.C., Andrews, B.D., and Flores, C., 2014, Seabed fluid expulsion along the upper slope and outer shelf of the U.S. Atlantic continental margin: Geophysical Research Letters, v. 41, p. 96–101, https://doi.org/10.1002/2013GL058048.

Brothers, D.S., Haeussler, P., East, A.E., ten Brink, U., Andrews, B., Dartnell, P., Miller, N., and Kluesner, J., 2017, A closer look at an undersea source of Alaskan earthquakes: Eos (Transactions, American Geophysical Union), v. 98, https://doi.org/10.1029/2017EO079019.

Brothers, D.S., Andrews, B.D., Walton, M.A.L., Greene, H.G., Barrie, J.V., Miller, N.C., ten Brink, U., East, A.E., Haeussler, P.J., Kluesner, J.W., and Conrad, J.E., 2019, Slope failure and mass transport processes along the Queen Charlotte Fault, southeastern Alaska, *in* Lintern, D.G., Mosher, D.C., Moscardelli, L.G., Bobrowsky, P.T., Campbell, C., Chaytor, J., Clague, J., Georgiopoulou, A., Lajeunesse, P., Normandeau, A., Piper, D., Scherwath, M., Stacey, C., and Turmel, D., eds., Subaqueous Mass Movements and Their Consequences: Assessing Geohazards, Environmental Implications and Economic Significance of Subaqueous Landslides: Geological Society of London Special Publication 477, p. 69–83, https://doi.org/10.1144/SP477.30.

Brothers, D.S., Miller, N.C., Barrie, J.V., Haeussler, P.J., Greene, H.G., Andrews, B.D., Zielke, O., Watt, J., and Dartnell, P., 2020, Plate boundary localization, slip-rates and rupture segmentation of the Queen Charlotte Fault based on submarine tectonic geomorphology: Earth and Planetary Science Letters, v. 530, 115882, https://doi.org/10.1016/j.epsl.2019.115882.

Bruns, T.R., and Carlson, P.R., 1987, Geology and petroleum potential of the southeast Alaska continental margin, *in* Scholl, D.W., Grantz, A., and Vedder, J.G., eds., Geology and Petroleum Potential of the Continental Margin of Western North America and Adjacent Ocean Basins: Beaufort Sea to Baja California: Circum-Pacific Council for Energy and Mineral Resources Earth Science Series Volume 6, p. 269–282.

Bullen, T.D., Krabbenhoft, D.P., and Kendall, C., 1996, Kinetic and mineralogic controls on the evolution of groundwater chemistry and $^{87}Sr/^{86}Sr$ in a sandy silicate aquifer, northern Wisconsin, USA: Geochimica et Cosmochimica Acta, v. 60, p. 1807–1821, https://doi.org/10.1016/0016-7037(96)00052-X.

Bünz, S., Polyanov, S., Vadakkepuliyambatta, S., Consolaro, C., and Mienert, J., 2012, Active gas venting through hydrate-bearing sediments on the Vestnesa Ridge, offshore W-Svalbard: Marine Geology, v. 332–334, p. 189–197, https://doi.org/10.1016/j.margeo.2012.09.012.

Campbell, K.A., 2006, Hydrocarbon seep and hydrothermal vent paleoenvironments and paleontology: Past developments and future research directions: Palaeogeography, Palaeoclimatology, Palaeoecology, v. 232, p. 362–407, https://doi.org/10.1016/j.palaeo.2005.06.018.

Carson, B., Holmes, M.L., Umstattd, K., Strasser, J.C., and Johnson, H.P., 1991, Fluid expulsion from the Cascadia accretionary prism: Evidence from porosity distribution, direct measurements, and GLORIA imagery: Philosophical Transactions of the Royal Society of London, Series A: Physical and Engineering Sciences, v. 335, p. 331–340, https://doi.org/10.1098/rsta.1991.0049.

Carson, B., Seke, E., Paskevich, V., and Holmes, M.L., 1994, Fluid expulsion sites on the Cascadia accretionary prism: Mapping diagenetic deposits with processed GLORIA imagery: Journal of Geophysical Research, v. 99, p. 11,959–11,969, https://doi.org/10.1029/94JB00120.

Chand, S., and Minshull, T.A., 2003, Seismic constraints on the effects of gas hydrate on sediment physical properties and fluid flow: A review: Geofluids, v. 3, p. 275–289, https://doi.org/10.1046/j.1468-8123.2003.00067.x.

Cheng, H., Edwards, R.L., Shen, C.C., Polyak, V.J., Asmerom, Y., Woodhead, J., Hellstrom, J., Wang, Y.J., Kong, X.G., Spötl, C., Wang, X.F., and Alexander, E.C., Jr., 2013, Improvements in $^{230}Th$ dating, $^{230}Th$ and $^{234}U$ half-life values, and U-Th isotopic measurements by multi-collector inductively coupled plasma mass spectrometry: Earth and Planetary Science Letters, v. 371–372, p. 82–91, https://doi.org/10.1016/j.epsl.2013.04.006.

Clague, J.J., 1983, Glacio-isostatic effects of the Cordilleran Ice Sheet, British Columbia, Canada, *in* Smith, D.E., and Dawson, A.G., eds., Shorelines and Isostasy: London, Academic Press, p. 321–343.

Claypool, G.E., Threlkeld, C.N., Mankiewicz, P.N., Arthur, M.A., and Anderson, T.F., 1985, Isotopic composition of interstitial fluids and origin of methane in slope sediment of the Middle America Trench, Deep Sea Drilling Project Leg 84, *in* von Huene, R., Aubouin, J., et al., Initial Reports of the Deep Sea Drilling Project, Volume 84: Balboa to Manzanillo: Washington, D.C., U.S. Government Printing Office, p. 683–691, https://doi.org/10.2973/dsdp.proc.84.124.1985.

Connolly, D.L., 2015, Visualization of vertical hydrocarbon migration in seismic data: Case studies from the Dutch North Sea: Interpretation (Tulsa), v. 3, no. 3, p. SX21–SX27, https://doi.org/10.1190/INT-2015-0007.1.

Conrad, J.E., Prouty, N.G., Walton, M.A.L., Kluesner, J.W., Maier, K.L., McGann, M., Brothers, D.S., Roland, E.C., and Dartnell, P., 2018, Seafloor fluid seeps on Kimki Ridge, offshore southern California: Links to active strike-slip faulting: Deep-Sea Research: Part II, Topical Studies in Oceanography, v. 150, p. 82–91, https://doi.org/10.1016/j.dsr2.2017.11.001.

Crémière, A., Bayon, G., Ponzevera, E., and Pierre, C., 2013, Paleo-environmental controls on cold seep carbonate authigenesis in the Sea of Marmara: Earth and Planetary Science Letters, v. 376, p. 200–211, https://doi.org/10.1016/j.epsl.2013.06.029.

Davidson, D.W., Leaist, D.G., and Hesse, R., 1983, Oxygen-18 enrichment in the water of a clathrate hydrate: Geochimica et Cosmochimica Acta, v. 47, p. 2293–2295, https://doi.org/10.1016/0016-7037(83)90053-4.

Davis, E.E., Becker, K., Wang, K., and Carson, B., 1995, Long-term observations of pressure and temperature in Hole 892B, Cascadia accretionary prism, *in* Carson, B., Westbrook, G.K., Musgrave, R.J., and Suess, E., eds., Proceedings of the Ocean Drilling Program, Scientific Results, Volume 146 (Part 1): College Station, Texas, Ocean Drilling Program, p. 299–311.

Depreiter, D., Poort, J., Van Rensbergen, P., and Henriet, J.P., 2005, Geophysical evidence of gas hydrates in shallow submarine mud volcanoes on the Moroccan margin: Journal of Geophysical Research, v. 110, B10103, https://doi.org/10.1029/2005JB003622.

Dickens, G.R., and Quinby-Hunt, M.S., 1994, Methane hydrate stability in seawater: Geophysical Research Letters, v. 21, p. 2115–2118, https://doi.org/10.1029/94GL01858.

Dimitrov, L.I., 2002, Mud volcanoes—The most important pathway for degassing deeply buried sediments: Earth-Science Reviews, v. 59, p. 49–76, https://doi.org/10.1016/S0012-8252(02)00069-7.

Dugan, B., and Flemings, P.B., 2002, Fluid flow and stability of the US continental slope offshore New Jersey from the Pleistocene to the present: Geofluids, v. 2, p. 137–146, https://doi.org/10.1046/j.1468-8123.2002.00032.x.

Dupré, S., Scalabrin, C., Grall, C., Augustin, J.-M., Henry, P., Şengör, A.M.C., Görür, N., Çağatay, M.N., and Géli, L., 2015, Tectonic and sedimentary controls on widespread gas emissions in the Sea of Marmara: Results from systematic, shipborne multibeam echo sounder water column imaging: Journal of Geophysical Research: Solid Earth, v. 120, p. 2891–2912, https://doi.org/10.1002/2014JB011617.

Edwards, R.L., Chen, J.H., and Wasserburg, G.J., 1987, $^{238}U$-$^{234}U$-$^{230}Th$-$^{232}Th$ systematics and the precise measurement of time over the past 500,000 years: Earth and Planetary Science Letters, v. 81, p. 175–192, https://doi.org/10.1016/0012-821X(87)90154-3.

Feng, D., Roberts, H.H., Cheng, H., Peckmann, J., Bohrmann, G., Lawrence Edwards, R., and Chen, D.F., 2010, U/Th dating of cold-seep carbonates: An initial comparison: Deep-Sea Research: Part II, Topical Studies in Oceanography, v. 57, p. 2055–2060, https://doi.org/10.1016/j.dsr2.2010.09.004.

Feng, D., Cheng, M., Kiel, S., Qiu, J.W., Yang, Q.H., Zhou, H.Y., Peng, Y.B., and Chen, D.F., 2015, Using *Bathymodiolus* tissue stable carbon, nitrogen and sulfur isotopes to infer biogeochemical process at a cold seep in the South China Sea: Deep-Sea Research: Part I, Oceanographic Research Papers, v. 104, p. 52–59, https://doi.org/10.1016/j.dsr.2015.06.011.

Fischer, D., Mogollón, J.M., Strasser, M., Pape, T., Bohrmann, G., Fekete, N., Spiess, V., and Kasten, S., 2013, Subduction zone earthquake as potential trigger of submarine hydrocarbon seepage: Nature Geoscience, v. 6, p. 647–651, https://doi.org/10.1038/ngeo1886.

Formolo, M.J., Lyons, T.W., Zhang, C.L., Kelley, C., Sassen, R., Horita, J., and Cole, D.R., 2004, Quantifying carbon sources in the formation of authigenic carbonates at gas hydrate sites in the Gulf of Mexico: Chemical Geology, v. 205, p. 253–264, https://doi.org/10.1016/j.chemgeo.2003.12.021.

Fossen, H., Schultz, R.A., Rundhovde, E., Rotevatn, A., and Buckley, S.J., 2010, Fault linkage and graben stepovers in the Canyonlands (Utah) and the North Sea Viking Graben, with implications for hydrocarbon migration and accumulation: American Association of Petroleum Geologists Bulletin, v. 94, p. 597–613, https://doi.org/10.1306/10130909088.

Gersztenkorn, A., and Marfurt, K.J., 1999, Eigenstructure-based coherence computations as an aid to 3-D structural and stratigraphic mapping: Geophysics, v. 64, p. 1468–1479, https://doi.org/10.1190/1.1444651.

Greene, H.G., O'Connell, V.M., Wakefield, W.W., and Brylinsky, C.K., 2007, The offshore Edgecumbe lava field, southeastern Alaska: Geologic and habitat characterization of a commercial fishing ground, *in* Todd, B.J., and Greene, H.G., eds.,



Downloaded from http://pubs.geoscienceworld.org/gsa/geosphere/article-pdf/16/6/1336/5182833/1336.pdf
by MBL WHOI Library user

Mapping the Seafloor for Habitat Characterization: Geological Association of Canada Special Paper 47, p. 277–296.
Greene, H.G., Barrie, J.V., Brothers, D.S., Conrad, J.E., Conway, K., East, A.E., Enkin, R., Maier, K.L., Nishenko, S.P., Walton, M.A.L., and Rohr, K.M.M., 2019, Slope failure and mass transport processes along the Queen Charlotte Fault Zone, western British Columbia, *in* Lintern, D.G., Mosher, D.C., Moscardelli, L.G., Bobrowsky, P.T., Campbell, C., Chaytor, J., Clague, J., Georgiopoulou, A., Lajeunesse, P., Normandeau, A., Piper, D., Scherwath, M., Stacey, C., and Turmel, D., eds., Subaqueous Mass Movements and their Consequences: Assessing Geohazards, Environmental Implications and Economic Significance of Subaqueous Landslides: Geological Society of London Special Publication 477, p. 85–106, https://doi.org/10.1144/SP477.31.
Greinert, J., Bohrmann, G., and Suess, E., 2001, Gas hydrate–associated carbonates and methane-venting at Hydrate Ridge: Classification, distribution, and origin of authigenic lithologies, *in* Paull, C.K., and Dillon, W.P., eds., Natural Gas Hydrates: Occurrence, Distribution, and Detection: American Geophysical Union Geophysical Monograph 124, p. 99–113, https://doi.org/10.1029/GM124p0099.
Grossman, E.L., and Ku, T.L., 1986, Oxygen and carbon isotope fractionation in biogenic aragonite: Temperature effects: Isotope Geoscience, v. 59, p. 59–74, https://doi.org/10.1016/0168-9622(86)90057-6.
Heggland, R., 2005, Using gas chimneys in seal integrity analysis: A discussion based on case histories, *in* Boult, P., and Kaldi, J., eds., Evaluating Fault and Cap Rock Seals: American Association of Petroleum Geologists Hedberg Series 2, p. 237–245.
Hein, J.R., Mizell, K., and Barnard, P.L., 2013, Sand sources and transport pathways for the San Francisco Bay coastal system, based on X-ray diffraction mineralogy: Marine Geology, v. 345, p. 154–169, https://doi.org/10.1016/j.margeo.2013.04.003.
Hensen, C., Wallmann, K., Schmidt, M., Ranero, C.R., and Suess, E., 2004, Fluid expulsion related to mud extrusion off Costa Rica—A window to the subducting slab: Geology, v. 32, p. 201–204, https://doi.org/10.1130/G20119.1.
Hensen, C., Duarte, J.C., Vannucchi, P., Mazzini, A., Lever, M.A., Terrinha, P., Géli, L., Henry, P., Villinger, H., Morgan, J., Schmidt, M., Gutscher, M.-A., Bartolome, R., Tomonaga, Y., Polonia, A., Gràcia, E., Tinivella, U., Lupi, M., Çağatay, M.N., Elvert, M., Sakellariou, D., Matias, L., Kipfer, R., Karageorgis, A.P., Ruffine, L., Liebetrau, V., Pierre, C., Schmidt, C., Batista, L., Gasperini, L., Burwicz, E., Neres, M., and Nuzzo, M., 2019, Marine transform faults and fracture zones: A joint perspective integrating seismicity, fluid flow and life: Frontiers of Earth Science, v. 7, https://doi.org/10.3389/feart.2019.00039.
Hyndman, R.D., 2015, Tectonics and structure of the Queen Charlotte fault zone, Haida Gwaii, and large thrust earthquakes: Bulletin of the Seismological Society of America, v. 105, p. 1058–1075, https://doi.org/10.1785/0120140181.
Hyndman, R.D., and Hamilton, T.S., 1993, Queen Charlotte Area Cenozoic tectonics and volcanism and their association with relative plate motions along the northeastern Pacific Margin: Journal of Geophysical Research, v. 98, p. 14,257–14,277, https://doi.org/10.1029/93JB00777.
Johnson, H.P., Miller, U.K., Salmi, M.S., and Solomon, E.A., 2015, Analysis of bubble plume distributions to evaluate methane hydrate decomposition on the continental slope: Geochemistry Geophysics Geosystems, v. 16, p. 3825–3839, https://doi.org/10.1002/2015GC005955.
Johnson, J.E., Goldfinger, C., and Suess, E., 2003, Geophysical constraints on the surface distribution of authigenic carbonates across the Hydrate Ridge region, Cascadia margin: Marine Geology, v. 202, p. 79–120, https://doi.org/10.1016/S0025-3227(03)00268-8.
Josenhans, H., Fedje, D., Pienitz, R., and Southon, J., 1997, Early humans and rapidly changing Holocene sea levels in the Queen Charlotte Islands–Hecate Strait, British Columbia, Canada: Science, v. 277, p. 71–74, https://doi.org/10.1126/science.277.5322.71.
Joseph, C., Campbell, K.A., Torres, M.E., Martin, R.A., Pohlman, J.W., Riedel, M., and Rose, K., 2013, Methane-derived authigenic carbonates from modern and paleoseeps on the Cascadia margin: Mechanisms of formation and diagenetic signals: Palaeogeography, Palaeoclimatology, Palaeoecology, v. 390, p. 52–67, https://doi.org/10.1016/j.palaeo.2013.01.012.
Judd, A.G., 2004, Natural seabed gas seeps as sources of atmospheric methane: Environmental Geology, v. 46, p. 988–996, https://doi.org/10.1007/s00254-004-1083-3.
Judd, A., and Hovland, M., 2007, Seabed Fluid Flow: The Impact on Geology, Biology and the Marine Environment: Cambridge, UK, Cambridge University Press, 475 p., https://doi.org/10.1017/CBO9780511535918.
Kastner, M., Elderfield, H., and Martin, J.B., 1991, Fluids in convergent margins: What do we know about their composition, origin, role in diagenesis and importance for oceanic chemical fluxes?: Philosophical Transactions of the Royal Society of London: Series A, Physical and Engineering Sciences, v. 335, p. 243–259, https://doi.org/10.1098/rsta.1991.0045.
Kiel, S., Birgel, D., Campbell, K.A., Crampton, J.S., Schiøler, P., and Peckmann, J., 2013, Cretaceous methane-seep deposits from New Zealand and their fauna: Palaeogeography, Palaeoclimatology, Palaeoecology, v. 390, p. 17–34, https://doi.org/10.1016/j.palaeo.2012.10.033.
Klasek, S.A., Torres, M.E., Loher, M., Bohrmann, G., Pape, T., and Colwell, F.S., 2019, Deep-sourced fluids from a convergent margin host distinct subseafloor microbial communities that change upon mud flow expulsion: Frontiers in Microbiology, v. 10, 1436, https://doi.org/10.3389/fmicb.2019.01436.
Kluesner, J.W., and Brothers, D.S., 2016, Seismic attribute detection of faults and fluid pathways within an active strike-slip shear zone: New insights from high-resolution 3D P-Cable™ seismic data along the Hosgri Fault, offshore California: Interpretation (Tulsa), v. 4, no. 1, p. SB131–SB148, https://doi.org/10.1190/INT-2015-0143.1.
Kluesner, J., Brothers, D., Hart, P., Miller, N., and Hatcher, G., 2018, Practical approaches to maximizing the resolution of sparker seismic reflection data: Marine Geophysical Researches, v. 40, p. 279–301, https://doi.org/10.1007/s11001-018-9367-2.
Kluesner, J.W., Silver, E.A., Bangs, N.L., McIntosh, K.D., Gibson, J., Orange, D., Ranero, C.R., and von Huene, R., 2013, High density of structurally controlled, shallow to deep water fluid seep indicators imaged offshore Costa Rica: Geochemistry Geophysics Geosystems, v. 14, p. 519–539, https://doi.org/10.1002/ggge.20058.
Kopf, A.J., 2002, Significance of mud volcanism: Reviews of Geophysics, v. 40, 1005, https://doi.org/10.1029/2000RG000093.
Kvenvolden, K.A., 1993, Gas hydrates—Geological perspective and global change: Reviews of Geophysics, v. 31, p. 173–187, https://doi.org/10.1029/93RG00268.
Lay, T., Ye, L.L., Kanamori, H., Yamazaki, Y., Cheung, K.F., Kwong, K., and Koper, K.D., 2013, The October 28, 2012 $M_w$ 7.8 Haida Gwaii underthrusting earthquake and tsunami: Slip partitioning along the Queen Charlotte Fault transpressional plate boundary: Earth and Planetary Science Letters, v. 375, p. 57–70, https://doi.org/10.1016/j.epsl.2013.05.005.
Levin, L.A., Baco, A.R., Bowden, D.A., Colaco, A., Cordes, E.E., Cunha, M.R., Demopoulos, A.W.J., Gobin, J., Grupe, B.M., Le, J., Metaxas, A., Netburn, A.N., Rouse, G.W., Thurber, A.R., Tunnicliffe, V., Van Dover, C.L., Vanreusel, A., and Watling, L., 2016, Hydrothermal vents and methane seeps: Rethinking the sphere of influence: Frontiers in Marine Science, v. 3, 72, https://doi.org/10.3389/fmars.2016.00072.
Liebetrau, V., Eisenhauer, A., and Linke, P., 2010, Cold seep carbonates and associated cold-water corals at the Hikurangi Margin, New Zealand: New insights into fluid pathways, growth structures and geochronology: Marine Geology, v. 272, p. 307–318, https://doi.org/10.1016/j.margeo.2010.01.003.
Ligtenberg, J.H., 2005, Detection of fluid migration pathways in seismic data: Implications for fault seal analysis: Basin Research, v. 17, p. 141–153, https://doi.org/10.1111/j.1365-2117.2005.00258.x.
Løseth, H., Gading, M., and Wensaas, L., 2009, Hydrocarbon leakage interpreted on seismic data: Marine and Petroleum Geology, v. 26, p. 1304–1319, https://doi.org/10.1016/j.marpetgeo.2008.09.008.
Maekawa, T., 2004, Experimental study on isotopic fractionation in water during gas hydrate formation: Geochemical Journal, v. 38, p. 129–138, https://doi.org/10.2343/geochemj.38.129.
Magalhães, V.H., Pinheiro, L.M., Ivanov, M.K., Kozlova, E., Blinova, V., Kolganova, J., Vasconcelos, C., McKenzie, J.A., Bernasconi, S.M., Kopf, A.J., Díaz-del-Río, V., González, F.J., and Somoza, L., 2012, Formation processes of methane-derived authigenic carbonates from the Gulf of Cadiz: Sedimentary Geology, v. 243–244, p. 155–168, https://doi.org/10.1016/j.sedgeo.2011.10.013.
Maloney, J.M., Grupe, B.M., Pasulka, A.L., Dawson, K.S., Case, D.H., Frieder, C.A., Levin, L.A., and Driscoll, N.W., 2015, Transpressional segment boundaries in strike-slip fault systems offshore southern California: Implications for fluid expulsion and cold seep habitats: Geophysical Research Letters, v. 42, p. 4080–4088, https://doi.org/10.1002/2015GL063778.
Mann, D., and Kukowski, N., 1999, Numerical modelling of focussed fluid flow in the Cascadia accretionary wedge: Journal of Geodynamics, v. 27, p. 359–372, https://doi.org/10.1016/S0264-3707(98)00008-8.
Marfurt, K.J., Sudhaker, V., Gersztenkorn, A., Crawford, K.D., and Nissen, S.E., 1999, Coherency calculations in the presence of structural dip: Geophysics, v. 64, p. 104–111, https://doi.org/10.1190/1.1444508.
Milkov, A.V., and Etiope, G., 2018, Revised genetic diagrams for natural gases based on a global dataset of >20,000 samples: Organic Geochemistry, v. 125, p. 109–120, https://doi.org/10.1016/j.orggeochem.2018.09.002.
Naehr, T.H., Eichhubl, P., Orphan, V.J., Hovland, M., Paull, C.K., Ussler, W., III, Lorenson, T.D., and Greene, H.G., 2007,


Downloaded from http://pubs.geoscienceworld.org/gsa/geosphere/article-pdf/16/6/1336/5182833/1336.pdf
by MBL WHOI Library user

Authigenic carbonate formation at hydrocarbon seeps in continental margin sediments: A comparative study: Deep-Sea Research: Part II, Topical Studies in Oceanography, v. 54, p. 1268–1291, https://doi.org/10.1016/j.dsr2.2007.04.010.

Paull, C.K., Ussler, W., III, Peltzer, E.T., Brewer, P.G., Keaten, R., Mitts, P.J., Nealon, J.W., Greinert, J., Herguera, J.-C., and Elena Perez, M., 2007, Authigenic carbon entombed in methane-soaked sediments from the northeastern transform margin of the Guaymas Basin, Gulf of California: Deep-Sea Research: Part II, Topical Studies in Oceanography, v. 54, p. 1240–1267, https://doi.org/10.1016/j.dsr2.2007.04.009.

Paull, C.K., Normark, W.R., Ussler, W., III, Caress, D.W., and Keaten, R., 2008, Association among active seafloor deformation, mound formation, and gas hydrate growth and accumulation within the seafloor of the Santa Monica Basin, offshore California: Marine Geology, v. 250, p. 258–275, https://doi.org/10.1016/j.margeo.2008.01.011.

Paull, C.K., Caress, D.W., Thomas, H., Lundsten, E., Anderson, K., Gwiazda, R., Riedel, M., McGann, M., and Herguera, J.C., 2015, Seafloor geomorphic manifestations of gas venting and shallow subbottom gas hydrate occurrences: Geosphere, v. 11, p. 491–513, https://doi.org/10.1130/GES01012.1.

Paytan, A., Kastner, M., Martin, E.E., Macdougall, J.D., and Herbert, T., 1993, Marine barite as a monitor of seawater strontium isotope composition: Nature, v. 366, p. 445–449, https://doi.org/10.1038/366445a0.

Peckmann, J., Birgel, D., and Kiel, S., 2009, Molecular fossils reveal fluid composition and flow intensity at a Cretaceous seep: Geology, v. 37, p. 847–850, https://doi.org/10.1130/G25658A.1.

Person, M., McIntosh, J., Bense, V., and Remenda, V.H., 2007, Pleistocene hydrology of North America: The role of ice sheets in reorganizing groundwater flow systems: Reviews of Geophysics, v. 45, RG3007, https://doi.org/10.1029/2006RG000206.

Petersen, C.J., Bünz, S., Hustoft, S., Mienert, J., and Klaeschen, D., 2010, High-resolution P-Cable 3D seismic imaging of gas chimney structures in gas hydrated sediments of an Arctic sediment drift: Marine and Petroleum Geology, v. 27, p. 1981–1994, https://doi.org/10.1016/j.marpetgeo.2010.06.006.

Pohlman, J.W., Kaneko, M., Heuer, V.B., Coffin, R.B., and Whiticar, M., 2009, Methane sources and production in the northern Cascadia margin gas hydrate system: Earth and Planetary Science Letters, v. 287, p. 504–512, https://doi.org/10.1016/j.epsl.2009.08.037.

Prouty, N.G., Sahy, D., Ruppel, C.D., Roark, E.B., Condon, D., Brooke, S., Ross, S.W., and Demopoulos, A.W.J., 2016, Insights into methane dynamics from analysis of authigenic carbonates and chemosynthetic mussels at newly-discovered Atlantic Margin seeps: Earth and Planetary Science Letters, v. 449, p. 332–344, https://doi.org/10.1016/j.epsl.2016.05.023.

Prouty, N.G., Lorenson, T.D., and Law, M.D., 2019, Geochemical analysis of seeps along the Queen Charlotte Fault: U.S. Geological Survey data release, https://doi.org/10.5066/P9RK94EE.

Reed, D.L., Silver, E.A., Tagudin, J.E., Shipley, T.H., and Vrolijk, P., 1990, Relations between mud volcanoes, thrust deformation, slope sedimentation, and gas hydrate, offshore north Panama: Marine and Petroleum Geology, v. 7, p. 44–54, https://doi.org/10.1016/0264-8172(90)90055-L.

Riedel, M., Rohr, K.M.M., Côté, M.M., Schmidt, U., and Richardson, T., 2020, Gas hydrate occurrences along the Haida Gwaii margin—Constraints on the geothermal regime and implications for fluid flow: Geosphere, v. 16, p. 1–12, https://doi.org/10.1130/GES02103.1.

Robinson, L.F., Belshaw, N.S., and Henderson, G.M., 2004, U and Th concentrations and isotope ratios in modern carbonates and waters from the Bahamas: Geochimica et Cosmochimica Acta, v. 68, p. 1777–1789, https://doi.org/10.1016/j.gca.2003.10.005.

Rohr, K.M.M., 2015, Plate boundary adjustment of the southernmost Queen Charlotte fault: Bulletin of the Seismological Society of America, v. 105, p. 1076–1089, https://doi.org/10.1785/0120140162.

Rohr, K.M.M., and Furlong, K.P., 1996, Ephemeral plate tectonics at the Queen Charlotte triple junction: Geology, v. 23, p. 1035–1038, https://doi.org/10.1130/0091-7613(1995)023<1035:EPTATQ>2.3.CO;2.

Rohr, K.M.M., Scheidhauer, M., and Trehu, A.M., 2000, Transpression between two warm mafic plates: The Queen Charlotte Fault revisited: Journal of Geophysical Research, v. 105, p. 8147–8172, https://doi.org/10.1029/1999JB900403.

Saffer, D.M., and Tobin, H.J., 2011, Hydrogeology and mechanics of subduction zone forearcs: Fluid flow and pore pressure: Annual Review of Earth and Planetary Sciences, v. 39, p. 157–186, https://doi.org/10.1146/annurev-earth-040610-133408.

Sahling, H., Masson, D.G., Ranero, C.R., Hühnerbach, V., Weinrebe, W., Klaucke, I., Bürk, D., Brückmann, W., and Suess, E., 2008, Fluid seepage at the continental margin offshore Costa Rica and southern Nicaragua: Geochemistry Geophysics Geosystems, v. 9, Q05S05, https://doi.org/10.1029/2008GC001978.

Sample, J.C., and Reid, M.R., 1998, Contrasting hydrogeologic regimes along strike-slip and thrust faults in the Oregon convergent margin: Evidence from the chemistry of syntectonic carbonate cements and veins: Bulletin of the Geological Society of America, v. 110, p. 48–59, https://doi.org/10.1130/0016-7606(1998)110<0048:CHRASS>2.3.CO;2.

Sauter, E.J., Muyakshin, S.I., Charlou, J.-L., Schlüter, M., Boetius, A., Jerosch, K., Damm, E., Foucher, J.-P., and Klages, M., 2006, Methane discharge from a deep-sea submarine mud volcano into the upper water column by gas hydrate–coated methane bubbles: Earth and Planetary Science Letters, v. 243, p. 354–365, https://doi.org/10.1016/j.epsl.2006.01.041.

Shen, C.C., Edwards, L.R., Cheng, H., Dorale, J.A., Thomas, R.B., Moran, S.B., Weinstein, S.E., and Edmonds, H.N., 2002, Uranium and thorium isotopic and concentration measurements by magnetic sector inductively coupled plasma mass spectrometry: Chemical Geology, v. 185, p. 165–178, https://doi.org/10.1016/S0009-2541(01)00404-1.

Shugar, D.H., Walker, I.J., Lian, O.B., Eamer, J.B.R., Neudorf, C., McLaren, D., and Fedje, D., 2014, Post-glacial sea-level change along the Pacific coast of North America: Quaternary Science Reviews, v. 97, p. 170–192, https://doi.org/10.1016/j.quascirev.2014.05.022.

Stakes, D.S., Orange, D., Paduan, J.B., Salamy, K.A., and Maher, N., 1999, Cold-seeps and authigenic carbonate formation in Monterey Bay, California: Marine Geology, v. 159, p. 93–109, https://doi.org/10.1016/S0025-3227(98)00200-X.

Stakes, D.S., Trehu, A.M., Goffredi, S.K., Naehr, T.H., and Duncan, R.A., 2002, Mass wasting, methane venting, and biological communities on the Mendocino transform fault: Geology, v. 30, p. 407–410, https://doi.org/10.1130/0091-7613(2002)030<0407:MWMVAB>2.0.CO;2.

Suess, E., 2014, Marine cold seeps and their manifestations: Geological control, biogeochemical criteria and environmental conditions: International Journal of Earth Sciences, v. 103, p. 1889–1916, https://doi.org/10.1007/s00531-014-1010-0.

Taylor, M.A., Hendy, I.L., and Pak, D.K., 2014, Deglacial ocean warming and marine margin retreat of the Cordilleran Ice Sheet in the North Pacific Ocean: Earth and Planetary Science Letters, v. 403, p. 89–98, https://doi.org/10.1016/j.epsl.2014.06.026.

Teichert, B.M.A., Eisenhauer, A., Bohrmann, G., Haase-Schramm, A., Bock, B., and Linke, P., 2003, U/Th systematics and ages of authigenic carbonates from Hydrate Ridge, Cascadia Margin: Recorders of fluid flow variations: Geochimica et Cosmochimica Acta, v. 67, p. 3845–3857, https://doi.org/10.1016/S0016-7037(03)00128-5.

Teichert, B.M.A., Gussone, N., Eisenhauer, A., and Bohrmann, G., 2005, Clathrites: Archives of near-seafloor pore-fluid evolution ($\delta^{44/40}$Ca, $\delta^{13}$C, $\delta^{18}$O) in gas hydrate environments: Geology, v. 33, p. 213–216, https://doi.org/10.1130/G21317.1.

Tingdahl, K.M., and de Groot, P.F.M., 2003, Post-stack dip- and azimuth processing: Journal of Seismic Exploration, v. 12, p. 113–126.

Tingdahl, K.M., Steen, Ø., Meldahl, P., and Ligtenberg, J.H., 2001, Semi-automatic detection of faults in 3-D seismic signals: Society of Exploration Geophysicists Technical Program Expanded Abstracts 2001, p. 1953–1956, https://doi.org/10.1190/1.1816520.

Tinivella, U., and Giustiniani, M., 2012, An overview of mud volcanoes associated to gas hydrate system, *in* Nemeth, K., ed., Updates in Volcanology: New Advances in Understanding Volcanic Systems: Rijeka, Croatia, InTech, p. 225–267, https://doi.org/10.5772/51270.

Tissot, B.P., and Welte, D.H., 1984, Petroleum Formation and Occurrence (second edition): Berlin, Springer-Verlag, 702 p., https://doi.org/10.1007/978-3-642-87813-8.

Torres, M.E., Embley, R.W., Merle, S.G., Tréhu, A.M., Collier, R.W., Suess, E., and Heeschen, K.U., 2009, Methane sources feeding cold seeps on the shelf and upper continental slope off central Oregon, USA: Geochemistry Geophysics Geosystems, v. 10, Q11003, https://doi.org/10.1029/2009GC002518.

Tréhu, A.M., Long, P.E., Torres, M.E., Bohrmann, G., Rack, F.R., Collett, T.S., Goldberg, D.S., Milkov, A.V., Riedel, M., Schultheiss, P., Bangs, N.L., Barr, S.R., Borowski, W.S., Claypool, G.E., Delwiche, M.E., Dickens, G.R., Gracia, E., Guerin, G., Holland, M., Johnson, J.E., Lee, Y.J., Liu, C.S., Su, X., Teichert, B., Tomaru, H., Vanneste, M., Watanabe, M., and Weinberger, J.L., 2004, Three-dimensional distribution of gas hydrate beneath southern Hydrate Ridge: Constraints from ODP Leg 204: Earth and Planetary Science Letters, v. 222, p. 845–862, https://doi.org/10.1016/j.epsl.2004.03.035.

Tréhu, A.M., Scheidhauer, M., Rohr, K.M.M., Tikoff, B., Walton, M.A.L., Gulick, S.P.S., and Roland, E.C., 2015, An abrupt transition in the mechanical response of the upper crust to transpression along the Queen Charlotte Fault: Bulletin of the Seismological Society of America, v. 105, p. 1114–1128, https://doi.org/10.1785/0120140159.

Tryon, M., Brown, K., Dorman, L., and Sauter, A., 2001, A new benthic aqueous flux meter for very low to moderate



Downloaded from http://pubs.geoscienceworld.org/gsa/geosphere/article-pdf/16/6/1336/5182833/1336.pdf
by MBL WHOI Library user

discharge rates: Deep-Sea Research: Part I, Oceanographic Research Papers, v. 48, p. 2121–2146, https://doi.org/10.1016/S0967-0637(01)00002-4.

Von Huene, R., Shor, G.G., Jr., and Wageman, J., 1979, Continental margins of the eastern Gulf of Alaska and boundaries of tectonic plates, *in* Watkins, J.S., Montadert, L., and Dickerson, P.W., eds., Geological and Geophysical Investigations of Continental Margins: American Association of Petroleum Geologists Memoir 29, p. 273–390.

Walton, M.A.L., Brothers, D.S., Miller, N.C., Kluesner, J., and Haeussler, P.J., 2018, Distribution of secondary faulting and deformation patterns along the Queen Charlotte Fault, southeastern Alaska: Abstract T51G-0259 presented American Geophysical Union Fall Meeting, Washington, D.C., 10–14 December.

Watson, S.J., Mountjoy, J.J., Barnes, P.M., Crutchley, G.J., Lamarche, G., Higgs, B., Hillman, J., Orpin, A.R., Micallef, A., Neil, H., Mitchell, J., Pallentin, A., Kane, T., Woelz, S., Bowden, D., Rowden, A.A., and Pecher, I.A., 2019, Focused fluid seepage related to variations in accretionary wedge structure, Hikurangi margin, New Zealand: Geology, v. 48, no. 1, p. 56–61, https://doi.org/10.1130/G46666.1.

Whiticar, M.J., 1999, Carbon and hydrogen isotope systematics of bacterial formation and oxidation of methane: Chemical Geology, v. 161, p. 291–314, https://doi.org/10.1016/S0009-2541(99)00092-3.

Whiticar, M.J., and Faber, E., 1986, Methane oxidation in sediment and water column environments—Isotope evidence: Organic Geochemistry, v. 10, p. 759–768, https://doi.org/10.1016/S0146-6380(86)80013-4.

Wood, W.T., Gettrust, J.F., Chapman, N.R., Spence, G.D., and Hyndman, R.D., 2002, Decreased stability of methane hydrates in marine sediments owing to phase-boundary roughness: Nature, v. 420, p. 656–660, https://doi.org/10.1038/nature01263.

Wood, W.T., Hart, P.E., Hutchinson, D.R., Dutta, N., Snyder, F., Coffin, R.B., and Gettrust, J.F., 2008, Gas and gas hydrate distribution around seafloor seeps in Mississippi Canyon, Northern Gulf of Mexico, using multi-resolution seismic imagery: Marine and Petroleum Geology, v. 25, p. 952–959, https://doi.org/10.1016/j.marpetgeo.2008.01.015.

Yue, H., Lay, T., Freymueller, J.T., Ding, K.H., Rivera, L., Ruppert, N.A., and Koper, K.D., 2013, Supershear rupture of the 5 January 2013 Craig, Alaska ($M_w$ 7.5) earthquake: Journal of Geophysical Research: Solid Earth, v. 118, p. 5903–5919, https://doi.org/10.1002/2013JB010594.



Downloaded from http://pubs.geoscienceworld.org/gsa/geosphere/article-pdf/16/6/1336/5182833/1336.pdf
by MBL WHOI Library user